

REPORT DOCUMENTATION PAGE			Form Approved OMB NO. 0704-0188		
<p>The public reporting burden for this collection of information is estimated to average 1 hour per response, including the time for reviewing instructions, searching existing data sources, gathering and maintaining the data needed, and completing and reviewing the collection of information. Send comments regarding this burden estimate or any other aspect of this collection of information, including suggestions for reducing this burden, to Washington Headquarters Services, Directorate for Information Operations and Reports, 1215 Jefferson Davis Highway, Suite 1204, Arlington VA, 22202-4302. Respondents should be aware that notwithstanding any other provision of law, no person shall be subject to any penalty for failing to comply with a collection of information if it does not display a currently valid OMB control number. PLEASE DO NOT RETURN YOUR FORM TO THE ABOVE ADDRESS.</p>					
1. REPORT DATE (DD-MM-YYYY) 13-10-2014		2. REPORT TYPE MS Thesis		3. DATES COVERED (From - To) -	
4. TITLE AND SUBTITLE Constitutive Behavior and Modeling of Al-Cu Alloy Systems			5a. CONTRACT NUMBER W911NF-10-1-0152		
			5b. GRANT NUMBER		
			5c. PROGRAM ELEMENT NUMBER 611102		
6. AUTHORS O. Anil Turkkan			5d. PROJECT NUMBER		
			5e. TASK NUMBER		
			5f. WORK UNIT NUMBER		
7. PERFORMING ORGANIZATION NAMES AND ADDRESSES Illinois Institute of Technology 3300 South Federal Street Room 301 Main Bldg Chicago, IL 60616 -3793			8. PERFORMING ORGANIZATION REPORT NUMBER		
9. SPONSORING/MONITORING AGENCY NAME(S) AND ADDRESS (ES) U.S. Army Research Office P.O. Box 12211 Research Triangle Park, NC 27709-2211			10. SPONSOR/MONITOR'S ACRONYM(S) ARO		
			11. SPONSOR/MONITOR'S REPORT NUMBER(S) 57429-EG.2		
12. DISTRIBUTION AVAILABILITY STATEMENT Approved for public release; distribution is unlimited.					
13. SUPPLEMENTARY NOTES The views, opinions and/or findings contained in this report are those of the author(s) and should not be construed as an official Department of the Army position, policy or decision, unless so designated by other documentation.					
14. ABSTRACT High speed deformation events such as caused by projectile penetration, fragment impact and shock/blast loading are of great importance in designing materials and structures for army applications. In these events, materials are subjected to large strains, high strain rates and rapid increase in temperature due to thermoplastic heating. In such severe conditions, overall performance is determined by the evolution of flow stress, failure initiation and propagation, and commonly in the form of adiabatic shear banding.					
15. SUBJECT TERMS Al-Cu alloys, high strain rate, constitutive modeling, rate and temperature dependent					
16. SECURITY CLASSIFICATION OF:		17. LIMITATION OF ABSTRACT		15. NUMBER OF PAGES	19a. NAME OF RESPONSIBLE PERSON
a. REPORT UU	b. ABSTRACT UU	c. THIS PAGE UU	UU		Murat Vural
				19b. TELEPHONE NUMBER 312-567-3181	

## Report Title

### Constitutive Behavior and Modeling of Al-Cu Alloy Systems

#### ABSTRACT

High speed deformation events such as caused by projectile penetration, fragment impact and shock/blast loading are of great importance in designing materials and structures for army applications. In these events, materials are subjected to large strains, high strain rates and rapid increase in temperature due to thermoplastic heating. In such severe conditions, overall performance is determined by the evolution of flow stress, failure initiation and propagation, and commonly in the form of adiabatic shear banding.

Some of 2XXX series aluminum-copper (Al-Cu) alloys are recognized for their decent ballistic properties, and therefore they have been used as an armor material for lightweight U.S. Army vehicles. Most recently, an Al-Cu-Mg-Mn-Ag alloy labeled as Al 2139-T8 has been developed and is evaluated by the U.S. Army Research Labs because of its better ballistic properties and higher strength than its predecessors. The underlying microstructure is believed to be the key element for this superior performance.

The goal of this study is to explore the effect of composition and microstructural features on overall dynamic material behavior by examining mechanical and deformation behavior of different Al-Cu material systems. Starting from the pure single crystal and polycrystalline Al structures, and adding a different element to chemical composition in each step (i.e., Cu, Mg, Mn, Ag), mechanical response of these different systems has been investigated. For all alloy systems with the exception of single crystal Al, mechanical tests have been performed at room and elevated temperatures covering quasi-static ( $10^{-3}$  to  $10^0$  s<sup>-1</sup>) and dynamic ( $10^2$  to  $10^4$  s<sup>-1</sup>) strain rate regimes.

Shear-compression specimens promoting localized shear deformation have been used to explore tendency of each one of these materials to failure by adiabatic shear banding.

In addition to phenomenological Johnson-Cook Model (JCM), physics based Zerrilli-Armstrong and Mechanical Threshold Models have been studied to model the constitutive response of Al-Cu alloys over a wide range of strain rates and temperatures.. An improved ZA model has been developed to better capture the trends in experimental data.

CONSTITUTIVE BEHAVIOR AND MODELING OF AL-CU ALLOY SYSTEMS

BY

OMER ANIL TURKKAN

DEPARTMENT OF MECHANICAL, MATERIALS, AND AEROSPACE  
ENGINEERING

Submitted in partial fulfillment of the  
requirements for the degree of  
Master of Science in Mechanical and Aerospace Engineering  
in the Graduate College of the  
Illinois Institute of Technology

Approved \_\_\_\_\_  
Adviser

Chicago, Illinois  
May 2013



## ACKNOWLEDGEMENT

First and foremost, I would like to thank my adviser, Professor Murat Vural for his support, encouragement, and supervision in my graduate studies. He is a true inspiration for my future academic career. I also thank him for aiding me financially with the research assistantship via U.S. Army Research Office at the Illinois Institute of Technology. I would like to thank Professor Sudhakar Nair and Professor Sammy Tin for serving as part of the thesis committee.

I would like to thank Henry Tran for teaching me all the experimental techniques. I also would like to thank my colleagues Saurabh Mathur, Yang Wang, Amlan Barua, Celal Evci and Mehmet Macar for turning work into a fun place and thus boosting me to endure the hard work. I, especially, want to express my deepest gratitude to Ravi Sastri Ayyagari for his unceasing support.

Notably, I would like to thank Russell Janota, Director of Operations in Mechanical, Materials and Aerospace Laboratories, for his guidance in setting up and maintaining complex testing apparatuses. I also would like to thank Craig Johnson, Machine Shop Supervisor, in machining specimens for my experiments.

Most importantly, I thank my parents and my sister for their full support and encouragement in carrying out this challenging journey. They are my biggest motivators to accomplish my utmost achievements.

## TABLE OF CONTENTS

	Page
ACKNOWLEDGEMENT .....	iii
LIST OF TABLES .....	vi
LIST OF FIGURES .....	vii
LIST OF SYMBOLS .....	xi
ABSTRACT .....	xiii
 CHAPTER	
1. INTRODUCTION .....	1
1.1 Motivation and Scope .....	1
1.2 The Alloys and Processing Techniques .....	3
1.3 Experimental Procedures .....	5
1.4 Adiabatic Shear Banding .....	15
1.5 Modified Johnson-Cook Model .....	17
1.6 Mechanical Threshold Model .....	20
1.7 Zerilli-Armstrong Model .....	26
2. EXPERIMENTAL RESULTS.....	29
2.1 Ultra-High Purity Single Crystal Aluminum .....	29
2.2 High-Purity Polycrystalline Aluminum .....	30
2.3 Solid Solution Aluminum Copper Alloy .....	31
2.4 Al-4.5%Cu Alloy .....	34
2.5 Al-4.5%Cu-0.5%Mg Alloy .....	35
2.6 Al-4.5%Cu-0.5%Mg-0.3%Mn Alloy.....	35
2.7 Al-4.5%Cu-0.5%Mg-0.3%Mn-0.3%Ag Alloy .....	38
3. MODIFIED ZERILLI-ARMSTRONG MODEL .....	40
3.1 Introduction.....	40
3.2 Former Modifications to ZA Model by Zerilli and Armstrong ..	42
3.3 Modifications to ZA Model .....	44

4. MODELING OF THE EXPERIMENTAL DATA.....	49
4.1 Introduction.....	49
4.2 [100] and [111] Single Crystals.....	50
4.3 Polycrystalline Aluminum .....	51
4.4 Al-0.1%Cu Alloy.....	53
4.5 Al-4.5%Cu-0.5%Mg-0.3%Mn-0.3%Ag Alloy.....	55
5. ADIABATIC SHEAR BANDING.....	58
5.1 Introduction .....	58
5.2 Parameter Fitting.....	58
5.3 Dynamic Testing.....	60
5.3 Stop-Ring Testing.....	60
6. DISCUSSION.....	62
6.1 Discussion .....	62
6.2 Recommendations for Future Work .....	63
APPENDIX	
A. MODELLING PARAMETERS .....	64
BIBLIOGRAPHY .....	67

## LIST OF TABLES

Table	Page
1.1. A summary of the tested alloys with their individual strengthening mechanisms and their processing procedure .....	4
A.1. Modified Johnson-Cook Model parameters for different materials.....	65
A.2. Zerilli-Armstrong Model parameters for different materials .....	65
A.3. Turkkán-Vural Modified Zerilli-Armstrong Model parameters for different materials .....	66

## LIST OF FIGURES

Figure	Page
1.1. M109 howitzer (left) and Marine Corps. Expeditionary Fighting Vehicle (right) are two examples of military vehicles utilizing aluminum-copper based armors which are subjected to harsh conditions. ....	1
1.2. The experimental test results of different aluminum alloys show that 2139 alloy has a higher minimum ultimate tensile strength and a better ballistic performance. (Placzankis and Charleton 2009) .....	2
1.3. The MTS quasi-static testing frame is shown after a high temperature test. Furnace door is open and the thermocouples are taken out. ....	6
1.4. Schematic of the SHPB setup.....	7
1.5. Schematic of the incident, transmitted, and reflected waves .....	7
1.6. Propagation of an elastic compressive wave in a thin cylindrical bar .....	8
1.7. A longitudinal wave reflects at the interface of two bars.....	10
1.8. Wave propagation in SHPB setup.....	12
1.9. One dimensional wave analysis in SHPB test.....	13
1.10. Defeat of armor by plugging is an example to formation of shear bands in dynamic deformation events. ....	16
1.11. Schematic of SCS geometry .....	17
2.1. On left force going into [111] orientation and on right going into [001] orientation of face-centered cubic structure. [Provided by H. Tran] .....	29
2.2. The material response of the two single crystals at quasi-static and dynamic regimes can be seen on the top row and the strain rate sensitivity of the two single crystals is presented at lower row. [Provided by H. Tran] .....	30
2.3. Comparison of the quasi-static performance of single crystalline and polycrystalline aluminum.....	31
2.4. In quasi-static regime solid solution aluminum copper alloy display slightly higher flow stress values at 0.1 strain offset; while in dynamic regime both materials have very similar flow stress values ( Also similar trends in elevated temperatures).....	31

2.5. Top row and lower left graphs show the material response of polycrystalline aluminum in different temperatures. Lower right graph demonstrates the strain rate sensitivity of the material in these temperatures at 0.1 strain value.	32
2.6. Top row and lower left graphs show the material response of solid solution aluminum copper alloy in different temperatures. Lower right graph demonstrates the strain rate sensitivity of the material in these temperatures at 0.1 strain offset value.	33
2.7. Room temperature experimental data for Al-4.5%Cu is shown. Since experiments are done till 3000/s strain rate, flow stress values are very similar in all experiments.	34
2.8. Comparison of Al-4.5%Cu and Al-4.5%Cu-0.5%Mg at the same strain rate. Addition of the Mg generates higher flow stress values.	35
2.9. Current progress in Al-4.5%Cu-0.5%Mg alloy is presented. Since only strain rates up to 3000/s have been covered, flow stress values in dynamic regime are not very different from the quasi-static flow stress values. Only quasi-static data is available at 220 C.	36
2.10. Comparison of the last three alloys in the dynamic regime. Al-4.5%Cu-0.5%Mg-0.3%Mn alloy has the highest flow stress values.	37
2.11. Room temperature data for the Al-4.5%Cu-0.5%Mg-0.3%Mn alloy is presented.	37
2.12. Room temperature and 220 C experimental data are presented at the upper row. Lower left graph show the thermal softening behavior. Lower right graph show all the experimental data in 0.15 strain offset.	38
2.13. Al-4.5%Cu 0.5%Mg-0.3%Mn -0.3%Ag alloy has the highest flow stress values among the other complex alloys. However after 0.3 strain, Al-4.5%Cu 0.5%Mg-0.3%Mn reaches the same flow stress value with the Ag alloy.	39
3.1. Polycrystalline aluminum shows hardening behavior akin to ZA model's hardening parameter, whereas aluminum-copper alloys show decreasing hardening rate with increasing strain rate.	41
3.2. Original Zerilli-Armstrong Model is used to model the Al-Cu-Mg-Mn-Ag alloy. Model fails to capture the increased strain-rate sensitivity in the dynamic regime.	42

3.3. Al-Cu-Mg-Mn-Ag alloy modeled with Modified Zerilli-Armstrong Model which shows increased strain-rate sensitivity in the dynamic regime. ....	45
3.4. Thermal softening of the flow stress is shown. After 500K, model behavior is very dissimilar to the experimental results. ....	46
3.5. TVZA model can successfully capture the softening behavior of the alloy even at temperatures above 500 K. ....	48
3.6. Al-Cu-Mg-Mn-Ag alloy modeled with Turkkan-Vural Modified Zerilli-Armstrong Model which shows increased strain-rate sensitivity in the dynamic regime. ....	48
4.1. Single Crystalline [111] direction aluminum modeled with original ZA Model. ....	50
4.2. Single Crystalline [111] and [011] direction aluminum modeled with original ZA Model. ....	51
4.3. Polycrystalline aluminum modeled with MJC Model. ....	52
4.4. Polycrystalline aluminum modeled with ZA Model. ....	53
4.5. Al-0.1%Cu modeled with MJC Model. ....	54
4.6. Al-0.1%Cu modeled with ZA Model. ....	55
4.7. Al-4.5%Cu-0.5%Mg-0.3%Mn-0.3%Ag modeled with MJC Model. ....	56
4.8. Al-4.5%Cu-0.5%Mg-0.3%Mn-0.3%Ag thermal softening captured with MJC Model. ....	56
4.9. Al-4.5%Cu-0.5%Mg-0.3%Mn-0.3%Ag modeled with TVZA Model. ....	57
4.10. Al-4.5%Cu-0.5%Mg-0.3%Mn-0.3%Ag thermal softening captured with TVZA Model. ....	57
5.1. Constants $k_1$ and $k_2$ are found by comparing quasi-static SCS and cylindrical experimental results. ....	58
5.2. Constants $k_1$ and $k_2$ are found by comparing quasi-static SCS and cylindrical experimental results. ....	59
5.3. Constants $k_1$ and $k_2$ are found by comparing quasi-static SCS and cylindrical experimental results. ....	59

5.4. SCS results of the three tested alloys. Strain rate is around 4000/s for all tests.....	60
5.5. Stop-ring SCS results of the three tested alloys. Strain rate is around 4000/s for all tests. ....	61

## LIST OF SYMBOLS

Symbol	Definition
ASB	Adiabatic shear band
$\widehat{\sigma}_a$	Athermal Component of Mechanical Threshold Stress
$\widehat{\sigma}_t$	Thermal Component of Mechanical Threshold Stress
$C_1$	Quasi-Static Strain Rate Sensitivity
$C_2$	Dynamic Strain Rate Sensitivity
$E_0$	Elastic modulus of SHPB Bar
$T_0$	Reference Temperature
$T_m$	Melting Temperature
$\varepsilon_{01}$	Reference Strain Rate
$\widehat{\sigma}$	Mechanical Threshold Stress
$\sigma_{th}$	Thermal Stress
Ag	Silver
Al	Aluminum
ARL	Army Research Lab.
C	Celcius
Cu	Copper
FCC	Face Centered Cubic
JC	Johnson-Cook
K	Kelvin
k	Microstructural Stress Intensty
Mg	Magnesium
MJC	Modified Johnson Cook
MMAE	Mechanical and Aerospace Engineering
Mn	Manganese
MTS	Mechanical threshold stress
MZA	Modified Zerilli-Armstrong Model

PID	Proportional-integral-derivative
SCS	Shear compression specimen
SHPB	Split Hopkinson Pressure Bar
T	Temperature
TVZA	Turkkan-Vural Modified Zerilli-Armstrong Model
ZA	Zerilli-Armstrong
$G$	Gibbs Free Energy
$\lambda$	Average Distance Travelled by Dislocations
$\mu$	Shear Modulus
$\rho$	Dislocation Density
$\omega$	Probability for annihilating a stopped dislocation

## ABSTRACT

High speed deformation events such as caused by projectile penetration, fragment impact and shock/blast loading are of great importance in designing materials and structures for army applications. In these events, materials are subjected to large strains, high strain rates and rapid increase in temperature due to thermoplastic heating. In such severe conditions, overall performance is determined by the evolution of flow stress, failure initiation and propagation, and commonly in the form of adiabatic shear banding.

Some of 2XXX series aluminum-copper (Al-Cu) alloys are recognized for their decent ballistic properties, and therefore they have been used as an armor material for lightweight U.S. Army vehicles. Most recently, an Al-Cu-Mg-Mn-Ag alloy labeled as Al 2139-T8 has been developed and is evaluated by the U.S. Army Research Labs because of its better ballistic properties and higher strength than its predecessors. The underlying microstructure is believed to be the key element for this superior performance.

The goal of this study is to explore the effect of composition and microstructural features on overall dynamic material behavior by examining mechanical and deformation behavior of different Al-Cu material systems. Starting from the pure single crystal and polycrystalline Al structures, and adding a different element to chemical composition in each step (i.e., Cu, Mg, Mn, Ag), mechanical response of these different systems has been investigated. For all alloy systems with the exception of single crystal Al, mechanical tests have been performed at room and elevated temperatures covering quasi-static ( $10^{-3}$  to  $10^0 \text{s}^{-1}$ ) and dynamic ( $10^2$  to  $10^4 \text{s}^{-1}$ ) strain rate regimes.

Shear-compression specimens promoting localized shear deformation have been used to explore tendency of each one of these materials to failure by adiabatic shear banding.

In addition to phenomenological Johnson-Cook Model (JCM), physics based Zerrilli-Armstrong and Mechanical Threshold Models have been studied to model the constitutive response of Al-Cu alloys over a wide range of strain rates and temperatures.. An improved ZA model has been developed to better capture the trends in experimental data.

## CHAPTER 1

### INTRODUCTION

#### 1.1 Motivation and Scope

Aluminum-copper (Al-Cu) alloys are broadly used in military and aerospace applications due to their relatively high strength, respectable ballistic performance and lower density value compared to other armor materials. Military vehicles shown in Figure 1.1 can be exposed to high strain rate and potentially localized deformation accompanied with rapid increase in temperature, and therefore armors made of Al-Cu alloys are expected to endure these extreme conditions.



Figure 1.1. M109 howitzer (left) and Marine Corps. Expeditionary Fighting Vehicle (right) are two examples of military vehicles utilizing aluminum-copper based armors which are subjected to harsh conditions.

2139 Al. alloy is recognized for its superior ballistic performance compared to other Al-Cu based alloys (Cho and Bes 2006) (Placzankis and Charleton 2009). In their paper, Placzankis and Charleton qualitatively showed this distinguished ballistic performance of 2139 alloy compared to other widely used Al. alloys which have decent ballistic properties (Fig.2). Although this notable performance in damage critical applications is well-known, the underlying mechanism for this behavior is not well

understood and requires a methodological study as a function of both composition and microstructural configuration. This study is an attempt to reveal the effect of such functions on the mechanical response of 2139 alloy.

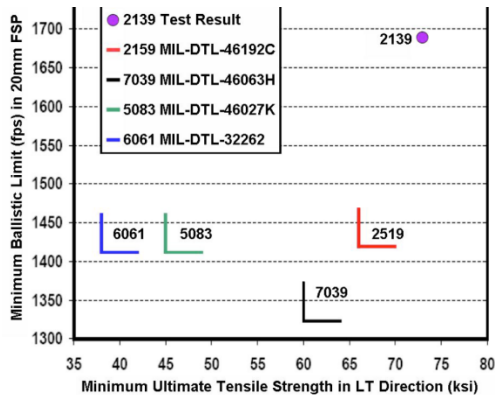


Figure 1.2. The experimental test results of different aluminum alloys show that 2139 alloy has a higher minimum ultimate tensile strength and a better ballistic performance. (Placzankis and Charleton 2009)

Current thesis study is composed of three major components as outlined below: (i) experimental investigation of rate and temperature dependent material behavior, (ii) understanding localized deformation behavior in the form of ASB, and (iii) constitutive modeling. Considering single crystalline and polycrystalline aluminum as base materials, a set of Al-Cu alloy systems is obtained by adding a different element in each stage (Table 1.1) and these alloys are tested in quasi-static and dynamic regime ( $10^{-3}\text{s}^{-1}$  to  $8000\text{ s}^{-1}$ ) at different temperatures (ranging from room temperature to  $320^\circ$ ) to discover their relative roles on strain hardening, strain rate sensitivity as well as their coupling with elevated temperatures.

In high strain rate deformation events such as ballistic penetration and blast loading, adiabatic shear banding (ASB) that is driven by the onset of thermoplastic deformation instabilities emerges as a the key deformation and failure mechanism. It was

found that the precipitates may have an important effect on the blocking ASB by acting as a barrier and also the adiabatic temperature rise is less than the matrix containing the precipitate (Elkhodary, et al. 2009). Therefore, due to its effect on ballistic properties, it is crucial to investigate the ASB phenomenon in different alloys to understand the influence of different precipitates. To introduce shear banding for experimental analysis, a shear compression specimen (SCS) was designed (Rittel, Lee and Ravichandran 2002) (Vural, Molinari and Bhattacharyya 2010). The SCS allows the material to experience large shear strains along a narrow gage section without geometric deformation instabilities (such as necking or barreling) and, therefore, is considered as one of a few specimen geometries suitable for exploring ASB.

Final part of the study consists of the constitutive modeling of the alloys that have been experimentally tested. These constitutive models act as a link between experimental and computational work. In addition to modeling the experimental data with purely phenomenological Johnson-Cook (JC) model (Johnson and Cook 1983), dislocation mechanics based the Mechanical Threshold Stress (MTS) (Follansbee and Kocks 1988) (Kocks, Realistic constitutive relations for metal plasticity 2001) and the Zerilli-Armstrong (ZA) model (Zerilli and Armstrong 1987) were employed to construct a dislocation based model that are capable of capturing experimental data with the least possible deviation over a wide range of strain, strain rate and temperature.

## **1.2 The Alloys and Processing Techniques**

This section describes the processing techniques for the alloys that are tested in this study. All alloys with the exception of single crystalline aluminum are prepared by our collaborative team in material science division led by Prof. S. Tin (Table 1.1).

Mechanical response of single crystal and polycrystalline aluminum was investigated by a former team member (H. Tran, MS Thesis, IIT) whose results are presented in this thesis study to provide a wider perspective. Single crystal aluminum was tested in the as-received state without any further processing. Polycrystalline aluminum specimens were extracted from a plate which was processed by cold rolling, and then annealing to refine the grain structure. All alloys were melted from high purity components by induction heating, and casted into a steel mold. Alloys containing Mg element were melted in an argon atmosphere to minimize oxidation. Precipitation hardenable alloys additionally aged at a low temperature of 320F to peak hardness. Each alloy were hot rolled and annealed to produce controlled grain refinement, and recrystallization kinetics of the various alloys was tracked (Snyder 2012).

Table 1.1. A summary of the tested alloys with their individual strengthening mechanisms and their processing procedure

Alloy (values in wt.%)	Strengthening Mechanism	Processed State
[100] and [111] Single Crystals	Inherent crystallography	Bridgman method, 6N purity
Polycrystalline Al	Grain boundaries	Rolled and recrystallized plate
Al-0.1Cu	Solid solution	Rolled and recrystallized plate
Al-4.5Cu	Heterogeneous precipitation of $\theta'$	Peak Aged at 160°C (320°F)
Al-4.5Cu-0.5Mg	More uniform, fine dispersion of $\theta'$	Peak Aged at 160°C (320°F)
Al-4.5Cu-0.5Mg-0.3Mn	$\theta'$ , $\text{Al}_{20}\text{Cu}_2\text{Mn}_3$ dispersoids	Peak Aged at 160°C (320°F)
Al-4.5Cu-0.5Mg-0.3Mn-0.3Ag	All above, plus $\Omega$ precipitation	Peak Aged at 160°C (320°F)

### 1.3 Experimental Procedure

**1.3.1 Quasi-Static Experiments.** To introduce strain rates ranging from  $10^{-3}$  to  $10^0$   $s^{-1}$ , a servo hydraulic test frame (with load capacity of 535kN)(Fig. 1.3) with MTS Flex Test SE Controller with high temperature MTS extensometers. For testing materials in this range, cylindrical specimens machined by MMAE Machine Shop with an L/D ratio of 1.2 were used. Due to small size of the specimens, the tested specimens were sandwiched between two alumina bars whose diameter is much greater than the specimen's diameter. Similarly because of the specimen size considerations, extensometer ends were attached to alumina bars and the displacement readings were taken from extensometer.

High temperature quasi-static tests were conducted using the same test frame and the only difference in the setup was the thermocouples attached to specimen's and alumina bars' surface via high temperature cement. A ceramic heater attached to the test frame was used to increase temperature of the specimen to the desired temperature. The three heating units inside the ceramic heater were controlled with a PID controller and the three thermocouples supplied the temperature readings for this process. An average heating sequence takes approximately ten minutes to reach 120 degrees Celsius and fifteen minutes to reach 220 degrees Celsius.



Figure 1.3. The MTS quasi-static testing frame is shown after a high temperature test. Furnace door is open and the thermocouples are taken out

**1.3.2 Dynamic Experiments.** The Split Hopkinson Pressure Bar (SHPB) setup was used to conduct high strain rate compression tests on Al-Cu materials and to obtain the stress-strain relationship based on stress wave data recorded from strain gages located on input and output bars. Figure 1.4 shows the schematic of the SHPB setup.

A striker bar launched from an air pressurized gun impacts the input bar and generates a compressive stress wave (incident wave) that propagates along the input bar. When the incident wave hits the interface between the specimen and the input bar, a portion of this wave reflects as a tensile wave (reflected wave), and the other compressive component is transmitted through specimen to output bar, thereby deforming the specimen during this high-speed process.

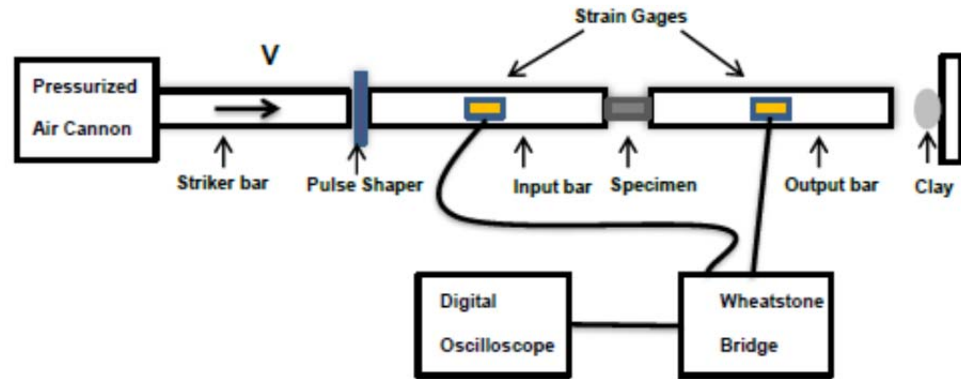


Figure 1.4. Schematic of the SHPB setup

Each of these stress waves (incident, transmitted, and reflected waves (Fig. 1.5)) are recorded through a high speed digital oscilloscope by using the signals from strain gages that are attached to the input and output bars. The stress waves are essential in determining dynamic stress-strain relationship of the specimen being tested.

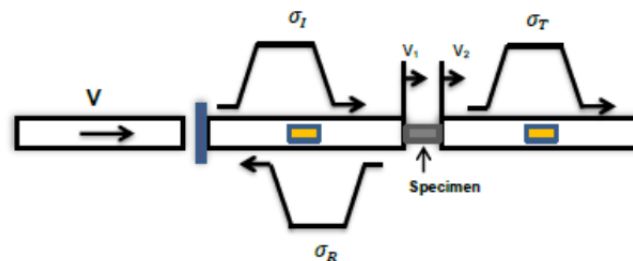


Figure 1.5. Schematic of the incident, transmitted, and reflected waves

These waves are essentially longitudinal elastic waves which correspond to the motion of the particles back and forth along the direction of wave propagation such that the particle velocity is parallel to the wave velocity. If the wave is compressive, they both have the same sense; if it is tensile, they have opposite sense (Meyers 1994).

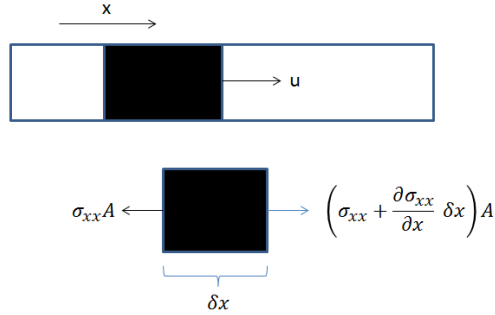


Figure 1.6. Propagation of an elastic compressive wave in a thin cylindrical bar

Suppose an elastic compressive wave is travelling through a bar's cross section with the velocity of  $c_0$  in the longitudinal direction, as shown in Fig. 1.6. According to the Newton's second law:

$$A \cdot \rho \delta x \cdot \frac{\partial^2 u}{\partial t^2} = A \left( \sigma_{xx} + \delta x \cdot \frac{\partial \sigma_{xx}}{\partial x} - \sigma_{xx} \right) \quad (1.1)$$

where  $A$  is the cross-sectional area of the bar,  $\rho$  is the density of the bar,  $\delta x$  is an infinitesimal length of the bar through which the wave is passing,  $u$  is the particle displacement, and  $\sigma_{xx}$  is the stress at the left side of the cross-section. After simplification:

$$\rho \cdot \frac{\partial^2 u}{\partial t^2} = \frac{\partial \sigma_{xx}}{\partial x} \quad (1.2)$$

The one dimensional (longitudinal direction) Hooke's Law is:

$$\begin{aligned} \sigma_{xx} &= E_0 \cdot \varepsilon \\ \sigma_{xx} &= E_0 \cdot \frac{\partial u}{\partial x} \end{aligned} \quad (1.3)$$

where  $E_0$  is the elastic modulus of the bar and the  $\varepsilon$  is the elastic strain in longitudinal direction. Substituting Eq. 1.3 into the Eq. 1.2 gives:

$$\rho \cdot \frac{\partial^2 u}{\partial t^2} = E \cdot \frac{\partial}{\partial x} \left( \frac{\partial u}{\partial x} \right)$$

$$\rho \cdot \frac{\partial^2 u}{\partial t^2} = E \cdot \frac{\partial^2 u}{\partial x^2} \quad (1.4)$$

The wave speed in the bar is related to the bar's density and elastic modulus as:

$$c_0 = \sqrt{\frac{E}{\rho}} \quad (1.5)$$

After substituting Eq. 1.5 into Eq. 1.4, one dimensional elastic wave equation in a thin bar can be obtained:

$$\frac{\partial^2 u}{\partial t^2} = c_0^2 \cdot \frac{\partial^2 u}{\partial x^2} \quad (1.6)$$

Before moving on to the SHPB equations, it would be worthwhile to study the behavior of the wave at the interfaces. D'Alembert's solution to the elastic wave equation is:

$$u = f(c_0 t - x) + F(c_0 t + x) \quad (1.7)$$

where  $u$  is the displacement,  $f$  is the wave travelling in the direction of increasing  $x$ ,  $F$  is the wave travelling in the direction of decreasing  $x$ . Considering a wave travelling in the direction of decreasing  $x$ :

$$u = F(c_0 t + x) \quad (1.8)$$

$$\frac{\partial u}{\partial x} = \frac{\partial F}{\partial (c_0 t + x)} \frac{\partial (c_0 t + x)}{\partial x} = F' \quad (1.9)$$

$$\frac{\partial u}{\partial t} = \frac{\partial F}{\partial (c_0 t + x)} \frac{\partial (c_0 t + x)}{\partial t} = F' c_0 \quad (1.10)$$

The last two equations show that partial differentiation of the displacement with respect to the distance and time can be related to each other as:

$$\frac{\partial u}{\partial x} = \frac{1}{c_0} \frac{\partial u}{\partial t} \quad (1.11)$$

Recalling that strain  $\varepsilon = \frac{\partial u}{\partial x}$ , particle velocity  $v = \frac{\partial u}{\partial t}$ , and substituting them into Eq. 1.11:

$$\varepsilon = \frac{1}{c_0} v \quad (1.12)$$

$$\frac{\sigma}{E} = \frac{1}{c_0} v$$

Finally, when Eq. 1.12 is substituted into Eq. 1.5:

$$\sigma = \rho c_0 v \quad (1.11)$$

When an incident wave of magnitude  $\sigma_I$  propagating along bar A, resulting in a particle velocity  $v_I$  reaches the interface between bars A and B, part of the wave with magnitude  $\sigma_T$  is transmitted to bar B, and the other part with magnitude  $\sigma_R$  is reflected back to bar A.

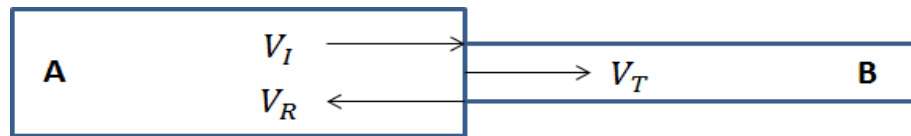


Figure 1.7. A longitudinal wave reflects at the interface of two bars

The force equilibrium between bars is:

$$A_A(\sigma_I + \sigma_R) = A_B \sigma_T \quad (1.12)$$

where  $A_A$  and  $A_B$  are the cross-sectional areas of the two bars. Due to velocity continuity:

$$v_I + v_R = v_T \quad (1.13)$$

Particle velocity can be linked to the stress in the bar according to the Eq. 1.11:

$$\begin{aligned}
v_I &= \frac{\sigma_I}{\rho_A c_A} \\
v_R &= -\frac{\sigma_R}{\rho_A c_A} \\
v_T &= \frac{\sigma_T}{\rho_B c_B}
\end{aligned} \tag{1.14}$$

where  $\rho$  and  $c$  are the density and the wave propagation speed, respectively. The negative sign for  $v_R$  is that a positive stress causes a negative particle velocity upon reflection and vice versa (Meyers 1994). When Eq. 1.14 is substituted to the Eq. 1.13:

$$\frac{\sigma_I}{\rho_A c_A} - \frac{\sigma_R}{\rho_A c_A} = \frac{\sigma_T}{\rho_B c_B} \tag{1.15}$$

From the equations 1.12 and 1.13:

$$\begin{aligned}
\frac{\sigma_T}{\sigma_I} &= \frac{2A_B \rho_B c_B}{A_B \rho_B c_B + A_A \rho_A c_A} \\
\frac{\sigma_R}{\sigma_I} &= \frac{A_B \rho_B c_B - A_A \rho_A c_A}{A_B \rho_B c_B + A_A \rho_A c_A}
\end{aligned} \tag{1.16}$$

where  $A\rho c$  is called the impedance of the bar.

When the impedance of the bar A is greater than that of bar B, the reflected wave is of the opposite sign to the incident wave and when it is less than the impedance of bar B, the reflected wave is of the same sign as the incident wave. However, no matter the impedances of the bars, the transmitted wave is always of the same sign as the incident wave.

Considering bar B as a free end with zero impedance and elastic modulus, the equations become:

$$\frac{\sigma_T}{\sigma_I} = 0$$

$$\frac{\sigma_R}{\sigma_I} = -1$$
(1.17)

So if a compressive wave is propagating to a free end, there will be no transmitted wave and the reflected wave is in tension with the same magnitude as the compressive wave. Another special case arises when bar B is considered as a rigid body with infinite elastic modulus:

$$\frac{\sigma_T}{\sigma_I} = 2$$

$$\frac{\sigma_R}{\sigma_I} = 1$$
(1.18)

Thus if a compressive wave is propagating to a rigid body, the reflected wave is also a compression wave with the same magnitude as the incident wave. Last special case is when the two bars have the same impedance:

$$\frac{\sigma_T}{\sigma_I} = 1$$

$$\frac{\sigma_R}{\sigma_I} = 0$$
(1.19)

As seen from these equations, when the two bars have the same impedance, there will be no reflected wave and the transmitted wave will have the same sign and magnitude with the incident wave.

SHPB setup consists of a compressive elastic stress wave propagating towards a sandwiched specimen whose impedance is smaller than that of the bars (Fig. 1.8).

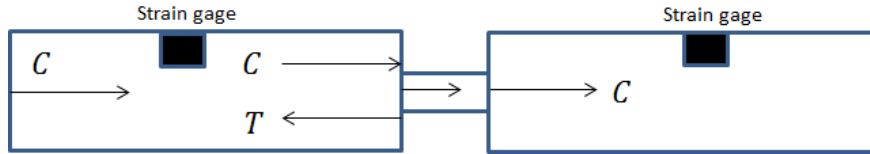


Figure 1.8. Wave propagation in SHPB setup

As the compressive stress wave, the incident wave, reaches the incident bar-specimen interface, part of it is reflected as tensile wave, called the reflected wave, because the bars have higher impedance than the specimen. The other part of the incident wave will be transmitted into the specimen as a compressive wave and when this wave reaches the specimen-transmitted bar interface, part of it will be reflected back into the specimen as a compressive wave due to specimen's smaller impedance. The rest of the wave will enter the transmitted bar as a compressive wave. Strain gage attached to the incident bar will record the incident wave and the reflected wave, whereas the other strain gage records the transmitted wave. D'Alembert's solution to the wave propagation in SHPB test (Fig 1.9) is:

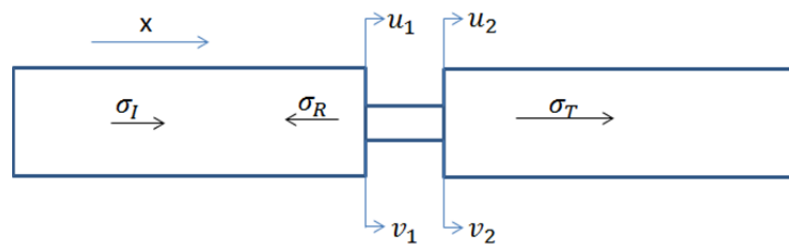


Figure 1.9. One dimensional wave analysis in SHPB test

$$\begin{aligned}
 u_1 &= f(x - c_0 t) + Fx + c_0 t = u_I + u_R \\
 u_2 &= g(x - c_0 t) = u_T
 \end{aligned}
 \tag{1.20}$$

When the last equation is differentiated with respect to  $x$ :

$$\begin{aligned}\varepsilon_1 &= f' + F' = \varepsilon_I + \varepsilon_R \\ \varepsilon_2 &= g' = \varepsilon_T\end{aligned}\tag{1.21}$$

Differentiating Eq. 1.20 with respect to time:

$$\begin{aligned}v_1 &= c_0(f' + F') = c_0(\varepsilon_I + \varepsilon_R) \\ v_2 &= -c_0g' = -c_0\varepsilon_T\end{aligned}\tag{1.22}$$

As the specimen is fairly shorter compared to the bars, it is practical to neglect the stress wave propagation in the specimen (Gray 2000). Then the engineering strain rate of the specimen is:

$$\begin{aligned}\dot{\varepsilon} &= \frac{v_1 - v_2}{L_s} \\ \dot{\varepsilon} &= \frac{c_0}{L_s}(-\varepsilon_I + \varepsilon_R + \varepsilon_T) \\ \dot{\varepsilon} &= \frac{c_0}{L_s E_0}(-\sigma_I + \sigma_R + \sigma_T)\end{aligned}\tag{1.23}$$

where  $L_s$  is the original specimen length,  $v_1$  and  $v_2$  are the particle velocities. The engineering strain can be found by integrating the strain rate:

$$\begin{aligned}\varepsilon_s &= \int^t \dot{\varepsilon} dt \\ &= \frac{c_0}{L_s E_0} \int^t (-\sigma_I + \sigma_R + \sigma_T) dt\end{aligned}\tag{1.24}$$

The engineering stress can be calculated by assuming that the force acting on specimen is the average of the two forces acting on the two interfaces:

$$\begin{aligned}
 F_1 &= A_0(\sigma_I + \sigma_R) \\
 F_2 &= A_0\sigma_T \\
 \sigma_s &= \frac{1}{2} \frac{F_1 + F_2}{A_s} \\
 &= \frac{A_0}{2A_s} (\sigma_I + \sigma_R + \sigma_T)
 \end{aligned} \tag{1.25}$$

Equations 1.24 and 1.25 are called three wave analysis because both of them employ all the three waves; incident, reflected, and transmitted waves. If the specimen is assumed to be in a stress equilibrium state, which can be obtained after a certain ringing up time which depends on the specimen properties, then the forces at the interfaces are equal to each other i.e.  $F_1 = F_2$ . Then  $\sigma_I + \sigma_R = \sigma_T$ , with this equilibrium condition, the three wave stress analysis can be reduced to one wave analysis:

$$\begin{aligned}
 \sigma_s &= \frac{A_0}{A_s} \sigma_T \\
 \varepsilon_s &= \frac{2c_0}{L_s E_0}
 \end{aligned} \tag{1.26}$$

All the derived equations are based on the one dimensional elastic wave propagation in the bars, for this assumption to be valid; several conditions should be satisfied (Gama, Lopatnikov and Jr. 2004):

- a) The bars are homogenous and isotropic.
- b) The bars are under elastic deformation.
- c) The bars are free of dispersion.

#### 1.4 Adiabatic Shear Banding

Adiabatic shear banding (ASB) is the major deformation mode in high-strain-rate deformation events, such as ballistic penetration and blast loading, it is particularly important in dynamic response and failure behavior parameters on the onset of thermoplastic deformation instabilities (Fig.1.10) (Meyers 1994).

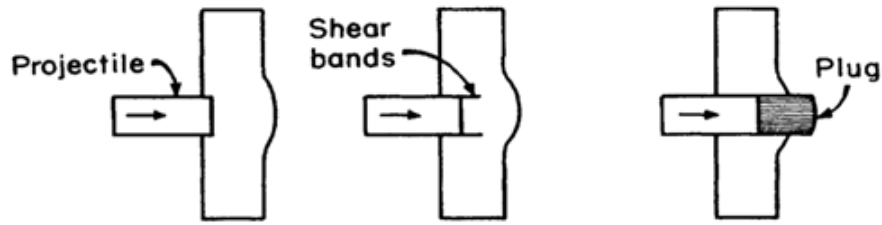


Figure 1.10. Defeat of armor by plugging is an example to formation of shear bands in dynamic deformation events.

Adiabatic shear band formation involves a narrow localized deformation band where very high shear strain takes place during dynamic deformation processes such that there is not enough time for thermoplastic heating to dissipate away from localized deformation site. This usually follows the situations where a bullet or a projectile has impacted a target material or during the manufacturing process where chipping, forging and upsetting can create unwanted adiabatic shear bands (Wright 2002). For aluminum materials adiabatic shear bands even occurred in cylindrical compression specimens (Wulf 1978).

A specialized specimen geometry, called shear-compression specimen (SCS), has been developed to study formation of ASB (Rittel, Lee and Ravichandran 2002) (Rittel, Ravichandran and Lee 2002). A cylindrical specimen geometry (Fig. 1.11), with two diametrically symmetric slots oriented with a specific degree to the axis of specimen was developed to stimulate uniform shear strain and stress distribution along the gage section.

More recently, the specimen geometry was improved by discovering that a slot angle of 35.26 degrees promotes the desired conditions in deformation of the gage section (Vural, Molinari and Bhattacharyya 2010).

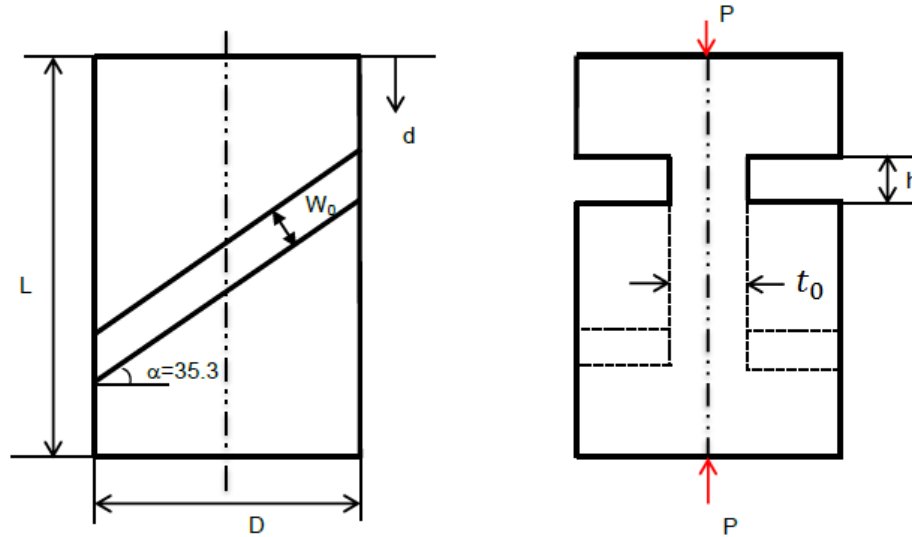


Figure 1.11. Schematic of SCS geometry

Equivalent stress and strain can be computed from the measured load and displacement as:

$$\varepsilon_{eq} = \frac{1}{k_1} \frac{\delta}{h} \quad (1.27)$$

$$\sigma_{eq} = k_1 \exp(-k_2 \varepsilon_{eq}) \frac{P}{Dt_0}$$

where  $\delta$  and  $P$  are measured displacement and force, respectively. The constants  $k_1$  and  $k_2$  are found by comparing cylindrical non-slotted specimen test with shear-compression specimen test, both of which are carried out at similar quasi-static strain rates.

### 1.5 Modified Johnson-Cook Model

The Johnson-Cook (JC) phenomenological plastic flow stress model is one of the most widely known temperature and strain rate dependent model and it is commonly used in computational codes (Johnson and Cook 1983). It has the following relation for the flow stress:

$$\sigma = [\sigma_0 + B(\varepsilon_p)^n] \left[ 1 + C \ln \left( \frac{\dot{\varepsilon}}{\dot{\varepsilon}_0} \right) \right] [1 - (T^*)^p] \quad (1.28)$$

where  $\varepsilon_p$  is the equivalent plastic strain,  $\dot{\varepsilon}$  is the strain rate,  $\dot{\varepsilon}_0$  is a user defined reference strain rate, and  $\sigma_0$ , B, n, C, p are material constants. The normalized temperature,  $T^*$ , is defined as:

$$T^* = \frac{T - T_0}{T_m - T_0} \quad (1.29)$$

where  $T_0$  is a reference temperature and  $T_m$  is a reference melting temperature in K. The success of JC model comes from multiplicative decomposition of strain hardening, strain rate hardening and thermal softening effects in three separate terms. Even if JC model is very flexible in modeling a variety of materials, it fails to capture the following behaviors of aluminum-copper alloys;

- The amount of strain hardening (B) decreases faster with increasing temperature than the predicted rate in JC model.
- The strain rate sensitivity in quasi-static regime increases with temperature, whereas JC model employs temperature independent strain rate sensitivity in quasi-static regime.

- Regardless of the temperature, there is a noteworthy dissimilarity in strain rate sensitivities of quasi-static and dynamic regime. However JC model predicts identical strain rate sensitivity in both regimes.

A modified Johnson-Cook Model (MJC) was developed to address these concerns in JC model (Vural and Caro 2009). The strain hardening term (B) was coupled with temperature as:

$$B = B_0[1 - (T^*)^p] \quad (1.30)$$

To resolve remaining issues in JC model, the strain rate sensitivity term (C) redefined as:

$$C = C_1(T_r^*)^q + C_2 H(\dot{\epsilon}, \dot{\epsilon}_t, k) \quad (1.31)$$

where

$$T_r^* = \frac{T - T_0}{T_r - T_0} \quad (1.32)$$

$$H(\dot{\epsilon}, \dot{\epsilon}_t, k) = \frac{1}{2} + \frac{1}{2} \tanh\left(k \ln \frac{\dot{\epsilon}}{\dot{\epsilon}_t}\right)$$

Here,  $\dot{\epsilon}_t$  represents the transition strain rate which separates the quasi-static and dynamic regime.  $H(\dot{\epsilon}, \dot{\epsilon}_t, k)$  function is a Heaviside step function that gives 1 when strain rate is greater than the transition rate and gives 0 when strain rate is smaller. Moreover by supplying continuous variation around the transition strain rate, this step function ensures a smooth transition between the two different strain rate regimes. Thanks to this step function, only  $C_1$  term dominates the quasi-static regime and also since it is coupled with temperature, it makes certain that there is increased rate sensitivity with increasing temperature in quasi-static regime. Furthermore,  $C_2$  can be chosen to be much greater than the  $C_1$  and thus dynamic regime can be controlled merely by  $C_2$  term. Lastly, due to

continuity in the flow stress at the end of quasi-static regime and at the beginning of dynamic regime requires that

$$\sigma_{qs} = \sigma_d \text{ at } \dot{\varepsilon} = \dot{\varepsilon}_t$$

$$\dot{\varepsilon}_0 = \dot{\varepsilon}_{01} \left\{ 1 + \left[ \left( \frac{\dot{\varepsilon}_t}{\dot{\varepsilon}_{01}} \right)^{\frac{C_2}{C_1(T_r^*)^q + C_2}} - 1 \right] H(\varepsilon_p, \dot{\varepsilon}, k) \right\} \quad (1.33)$$

where  $\dot{\varepsilon}_{01}$  is the reference strain rate.

## 1.6 Mechanical Threshold Model

Mechanical Threshold Stress (MTS) model is a dislocation based material model which incorporates mechanical threshold stress as a state variable (Follansbee and Kocks 1988) (Follansbee, Kocks and Regazzoni 1985) (Kocks, Realistic constitutive relations for metal plasticity 2001). . To comprehend the meaning of the mechanical threshold stress, a thought experiment can be carried out at 0 K. If an increasing amount of shear stress is applied to a nearly perfect crystal containing the necessary defects for deformation, there would be no detectable shear strain rate until  $\sigma = \hat{\tau}(0)$ . At this shear stress, the shear strain rate will approach an inertially limited strain rate, and this material property  $\hat{\tau}(0)$  is called as the mechanical threshold for initiating deformation by a specific mechanism, such as the intrinsic lattice resistance to dislocation glide or resistance to dislocation glide caused by a field of solute atoms, precipitate particles. Therefore this idealization can be summarized at 0 K as:

$$\begin{aligned} \dot{\gamma} &= 0 \text{ for } \sigma < \hat{\tau}(0), \\ \dot{\gamma} &> 0 \text{ for } \sigma = \hat{\tau}(0). \end{aligned} \quad (1.34)$$

also  $\sigma = \hat{\tau}(0)$  is unattainable under quasi-static conditions.

When temperature is greater than zero Kelvin, this behavior will change in two ways. Since the resistance to deformation is governed by the elastic interaction on atomic

level, temperature dependence of the elastic constants.(Where is the sentence here?) Similarly, with increasing temperature, local energy barriers can be overcome at lower shear stress with the help of the local temperature fluctuations.

The Mechanical Threshold Stress Model uses this mechanical threshold stress (flow stress at 0 K) as a state parameter to calculate the flow stress. The mechanical threshold stress is separated into two components,

$$\hat{\sigma} = \hat{\sigma}_a + \hat{\sigma}_t \quad (1.35)$$

where  $\sigma_a$  represents the rate independent interactions of dislocations with long range barriers such as grain boundaries whereas  $\hat{\sigma}_t$  represents the rate dependent interactions with short range obstacles. The flow stress at temperatures greater than 0 K, the flow stress will be:

$$\sigma = \hat{\sigma}_a + \sigma_t = \hat{\sigma}_a + s(\dot{\epsilon}, T) \hat{\sigma}_t \quad (1.36)$$

If the rate controlling deformation mechanism is thermal activation, then the contribution of thermal activation energy will reduce the stress required for a dislocation to pass a barrier. Thus the factor S always will be less than 1. The kinetics of thermally activated glide is described by the Arrhenius expression of the form:

$$\dot{\epsilon} = \dot{\epsilon}_0 \exp \left[ \frac{\Delta G(\sigma_t, \hat{\sigma}_t)}{kT} \right] \quad (1.37)$$

For the free energy  $\Delta G$ , a phenomenological relation is selected:

$$\Delta G = g_0 \mu b^3 \left[ 1 - \left( \frac{\sigma_t}{\hat{\sigma}_t} \right)^p \right]^q \quad (1.38)$$

where  $g_0$  is the normalized activation energy, which is assumed to remain constant as long as obstacle character is same,  $\mu$  is the shear modulus,  $b$  is the magnitude of Burgers vector, and  $p$  and  $q$  are constants that characterize the obstacle profile. For different

materials and for different heat treatments for the same material p and q are different. If last three equations are rearranged, the equation for flow stress will be:

$$\sigma = \hat{\sigma}_a + (\hat{\sigma} - \hat{\sigma}_a) \left\{ 1 - \left[ \frac{kT \ln \left( \frac{\dot{\epsilon}_0}{\dot{\epsilon}} \right) \right]^{\frac{1}{q}} \right\}^{\frac{1}{p}} \quad (1.39)$$

This equation gives the flow stress value for a given structure ( $\hat{\sigma}$ ), thus investigating the evolution of the structure is necessary for obtaining stress strain curves.

MTS model uses Kocks-Mecking(KM) model (Kocks 1976) for predicting the evolution of the structure with the strain. This approach assumes that the kinetics of plastic flow is determined by a single structure parameter S representing the current structure. At a given structure, flow stress can be represented as:

$$\Delta\sigma = \sigma(S, \dot{\epsilon}, T) \quad (1.40)$$

Evolution of the structure with strain  $\varepsilon$  at a given temperature and strain rate is:

$$\frac{dS}{d\varepsilon} = f(S, \dot{\epsilon}, T) \quad (1.41)$$

It is also assumed that the structure parameter S evolves towards a saturation value  $S_S$ . Thus, the flow stress  $\sigma$  evolves towards a saturation or steady state of value  $\sigma_S$ .  $\sigma_S$  can be expressed as a function of temperature and strain rate as  $\sigma_S = \sigma_S(\dot{\epsilon}, T)$ .

MTS model chooses the mechanical strength of obstacles to dislocation glide,  $\hat{\sigma}$ , as the structure parameter which is related to dislocation density as:

$$\hat{\sigma} = \alpha\mu b\rho^{\frac{1}{2}} \quad (1.42)$$

where  $\mu$  is the shear modulus,  $b$  is the magnitude of the Burgers vector and  $\alpha$  is a numerical constant of order unity. The KM model has the equation for the evolution of dislocation density,  $\rho$ , as:

$$\frac{d\rho}{d\varepsilon} = k_1\rho^{\frac{1}{2}} - k_2\rho \quad (1.43)$$

The  $k_1\rho^{\frac{1}{2}}$  term is associated with the athermal ( $k_1$ =constant) storage of moving dislocations which become immobilized after having travelled a distance proportional to average spacing between dislocations,  $\rho^{\frac{1}{2}}$ .  $k_2\rho$  is the dynamic recovery by dislocation annihilation and cross slip of the dislocations. Since dynamic recovery is thermally activated,  $k_2$  is a function of temperature and strain rate.

By combining the last two equations, the evolution equation for the structure can be found as:

$$\frac{d\hat{\sigma}}{d\varepsilon} = \theta \left( 1 - \frac{\hat{\sigma}}{\hat{\sigma}_s} \right) \quad (1.44)$$

with

$$\theta = \frac{\alpha\mu bk_1}{2} \quad (1.45)$$

$$\hat{\sigma}_s = \alpha\mu b \left( \frac{k_1}{k_2} \right)$$

According to the KM model  $\theta$  does not change with strain rate and has temperature dependence through  $\mu$  term. Also according to this equation,  $\hat{\sigma}$  evolves towards a steady state value,  $\hat{\sigma}_s$  where strain hardening is zero. The MTS model did not employ the KM hardening model without any modifications. First to have a better fit to the data, it has been modified to:

$$\theta = \theta_0 \left[ 1 - F \left( \frac{\hat{\sigma} - \hat{\sigma}_a}{\hat{\sigma}_s - \hat{\sigma}_a} \right) \right] \quad (1.46)$$

The function  $F$  is selected to fit the measured data. Another deviation from the original KM hardening model is that the athermal hardening coefficient  $\theta_0$  is found to have a strain rate dependency from the experimental data in FCC materials. Thus, it is assumed have a form such as:

$$\theta_0 = A + B \ln(\dot{\epsilon}) + C \dot{\epsilon} \quad (1.47)$$

The KM hardening model assumes the dislocations move a distance,  $d$ , proportional to the average distance between dislocations. But at very high strain rates, the dislocation immobilization distance is simply the distance that a dislocation can move during the imposed time duration of deformation. Also, this increase in athermal strain rate with strain rate may be the reason for the increased strain rate sensitivity in dynamic region for fcc materials. Finally, an Arrhenius type of equation is proposed for saturation stress:

$$\ln \left( \frac{\dot{\epsilon}}{\dot{\epsilon}_{s0}} \right) = \frac{\mu b^3 A}{kT} \ln \left( \frac{\hat{\sigma}_s}{\hat{\sigma}_{s0}} \right) \quad (1.48)$$

where  $\dot{\epsilon}_{s0}$ ,  $\hat{\sigma}_{s0}$ ,  $A$  are constants and  $\hat{\sigma}_s$  is the saturation threshold stress for deformation at 0 K.

After recent modifications, latest form of the MTS model is (Banerjee 2007):

$$\sigma = \sigma_a + (S_i \sigma_i + S_e \sigma_e) \frac{\mu(p, T)}{\mu_0} \quad (1.49)$$

where  $\sigma_a$  is the athermal component of stress,  $\sigma_i$  is the intrinsic component of the flow stress,  $\sigma_e$  is the strain hardening component of the flow stress,  $S_i$  and  $S_e$  are strain rate and temperature dependent scaling factors, and  $\mu_0$  is the shear modulus at 0 K and ambient pressure. Parallel to the original MTS model (Eq.1.39), scaling factors have Arrhenius form:

$$S_i = \left\{ 1 - \left[ \frac{kT \ln \left( \frac{\dot{\epsilon}_{oi}}{\dot{\epsilon}} \right)^{\frac{1}{q_i}}}{g_{oi} \mu b^3} \right] \right\}^{\frac{1}{p_i}}$$

$$S_e = \left\{ 1 - \left[ \frac{kT \ln \left( \frac{\dot{\epsilon}_{oe}}{\dot{\epsilon}} \right)^{\frac{1}{q_e}}}{g_{oe} \mu b^3} \right] \right\}^{\frac{1}{p_e}}$$
(1.50)

where  $g_{oi,e}$  is the normalized activation energy,  $\mu$  is the shear modulus,  $b$  is the magnitude of Burgers vector,  $\dot{\epsilon}_{oi,e}$  are the reference strain rates, and  $p_{i,e}$  and  $q_{i,e}$  are constants that characterize the obstacle profile.

Hardening is kept same as the original equation with the addition of saturation hardening:

$$\frac{d\sigma_e}{d\varepsilon} = \theta_0 [1 - F(\sigma_e)] + \theta_1 F(\sigma_e)$$

$$\theta_0 = a_{00} + a_{10} \ln \dot{\epsilon} + a_{20} \sqrt{\dot{\epsilon}} + a_{30} T$$

$$\theta_1 = a_{01} + a_{11} \ln \dot{\epsilon} + a_{21} \sqrt{\dot{\epsilon}} + a_{31} T$$
(1.51)

$$F(\sigma_e) = \frac{\tanh\left(\alpha \frac{\sigma_e}{\sigma_s}\right)}{\tanh(\alpha)}$$

$$\ln\left(\frac{\dot{\epsilon}}{\dot{\epsilon}_{s0}}\right) = \frac{\mu b^3 A}{kT} \ln\left(\frac{\sigma_{es}}{\sigma_{e0s}}\right)$$

where  $\theta_0$  is the hardening rate,  $\theta_1$  is hardening rate at saturation,  $a_{ij}$ , and  $\alpha$  are constants,  $\dot{\epsilon}_{s0}$ ,  $\sigma_{es}$ ,  $A$  are constants at zero strain hardening rate and  $\sigma_{e0s}$  is the saturation threshold stress for deformation at 0 K.

### 1.7 Zerilli-Armstrong Model

The Zerilli-Armstrong (ZA) model (Zerilli and Armstrong 1987) (Zerilli and Armstrong 1997) (Zerilli 2004)) is based on simplified dislocation mechanics. Dislocation model basis for plastic shear strain-rate is:

$$\dot{\gamma} = m' b \rho v \quad (1.52)$$

where  $m'$  is a tensor orientation factor,  $\rho$  is the dislocation density,  $b$  is the Burgers vector and  $v$  is the average dislocation velocity. Average dislocation velocity is governed by thermally activated processes to overcome local obstacles:

$$v = v_0 \exp\left(-\frac{G}{kT}\right) \quad (1.53)$$

where  $v_0$  is the reference dislocation velocity,  $G$  is the Gibbs free energy of activation,  $k$  is the Boltzmann constant, and  $T$  is the absolute temperature.  $G$  can be expressed as:

$$G = G_0 - \int_0^{\tau_{th}} A^* b d\tau'_{th} \quad (1.54)$$

where  $G_0$  is the reference Gibbs energy at  $T=0$ ,  $A^*$  is the area of activation, and  $\tau'_{th}$  is the thermal component of the shear stress. Mean value of  $A^* b$  can be expressed as:

$$\langle Ab \rangle = \left(\frac{1}{\tau_{th}}\right) \int_0^{\tau_{th}} A^* b d\tau'_{th} \quad (1.54)$$

Eq. 1.52 to Eq.1.54 can be expressed in an alternative for, keeping in mind that  $\sigma_{th} = m \tau_{th}$  and  $\epsilon = \frac{\gamma}{m}$ :

$$\sigma_{th} = B e^{-\beta T} \quad (1.55)$$

where

$$B = \frac{mG_0}{A_0b}$$

$$\beta = \left(\frac{1}{T}\right) \ln\left(\frac{A}{A_0}\right) - \left(\frac{1}{T}\right) \ln\left(1 + \left(\frac{kT}{G_0}\right) \ln\left(\frac{\dot{\epsilon}}{\dot{\epsilon}_0}\right)\right) \quad (1.56)$$

The B term is the threshold stress and it is reduced by  $e^{-\beta T}$  factor to calculate the flow stress. Using the expansion  $\ln(1 + x) \approx x$ , the  $\beta$  term can be written as:

$$\beta = \beta_0 - \beta_1 \ln(\dot{\epsilon}) \quad (1.57)$$

Activation area (A) is a measure of the separation distance, d, between the dislocations such as:

$$A^* \cong \frac{db}{2} \quad (1.58)$$

Also it is known that average dislocation separation (d) is related to dislocation density ( $\rho$ ) as:

$$\rho \sim \frac{1}{d^2} \quad (1.59)$$

Using Eq.1.59, activation area can be related to dislocation density:

$$A \sim \frac{1}{\sqrt{\rho}} \quad (1.60)$$

Considering the relation between strain and dislocation density at 0 K:

$$A \sim \frac{1}{\sqrt{\epsilon}} \quad (1.61)$$

Finally activation energy can be described with following relation:

$$A = \frac{A'_0}{\sqrt{\epsilon}} \quad (1.62)$$

Thus, for the fcc case, thermal component of the stress can be expressed as:

$$\sigma_{th} = c_1\sqrt{\epsilon} \exp(-c_2T + c_3T\ln\dot{\epsilon}) \quad (1.63)$$

There will be an effect of the grain boundaries on the stress and ZA model covers this effect by adding an athermal component of stress to the model:

$$\sigma_a = \frac{k}{\sqrt{l}} + \sigma_s \quad (1.64)$$

Where k is the microstructural stress intensity, l is the average grain diameter and  $\sigma_s$  is the stress increase due to solutes. Final form of the ZA model is:

$$\sigma = c_1\sqrt{\epsilon} \exp(-c_2T + c_3T\ln\dot{\epsilon}) + \frac{k}{\sqrt{l}} + \sigma_s \quad (1.65)$$

Zerilli (Zerilli 2004) modified this equation to include both Peierls stress type interactions and interaction of forest-dislocations type interactions:

$$\sigma = \sigma_a + B e^{-\beta T} + B_0 \epsilon^{\frac{1}{2}} e^{-\alpha T} \quad (1.66)$$

where

$$\alpha = \alpha_0 - \alpha_1 \ln(\dot{\epsilon})$$

$$\beta = \beta_0 - \beta_1 \ln(\dot{\epsilon}) \quad (1.67)$$

$$\sigma_a = \frac{k}{\sqrt{l}} + \sigma_s$$

CHAPTER 2  
EXPERIMENTAL RESULTS

### 2.1 Ultra-High-Purity Single Crystal Aluminum

As a first step in this study, uniaxial compression tests were conducted in quasi-static and dynamic regimes at room temperature in ultra-high-purity single crystal aluminum in the  $[111]$  and  $[001]$  orientations (Tran 2011)(Fig. 3.1)(Fig 3.2).

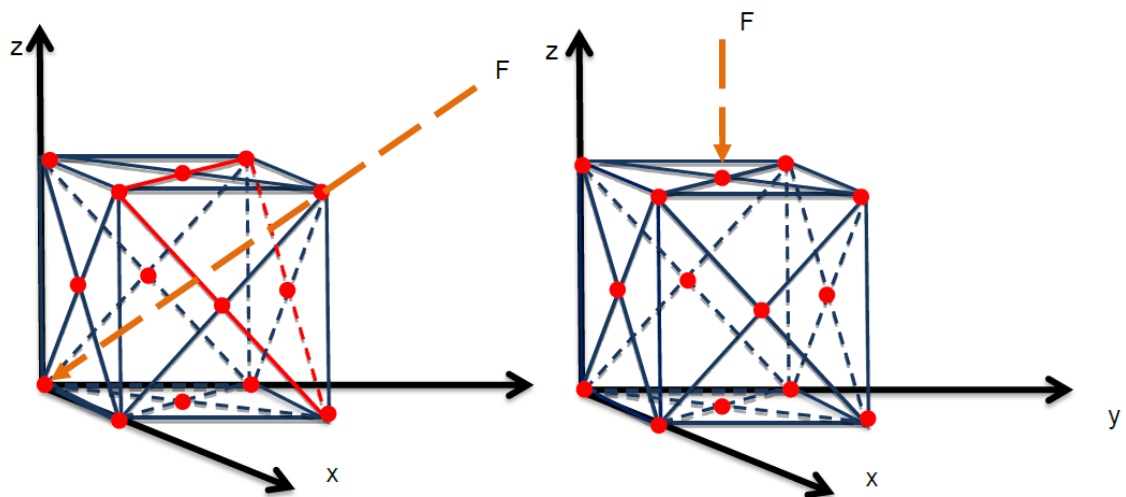


Figure 2.1. On left force going into  $[111]$  orientation and on right going into  $[001]$  orientation of face-centered cubic structure. [Provided by H. Tran]

As figure 2.2 shows that the  $[111]$  orientation single crystal has twice as larger flow stress values compared to  $[001]$  orientation single crystal at a given strain value. Also both orientations show increased rate sensitivity in dynamic region. They show continuous strain hardening without saturation at large strain values. Since there were limited number of single crystal aluminum specimens, no high temperature tests were done, thus this material was not characterized at elevated temperatures.

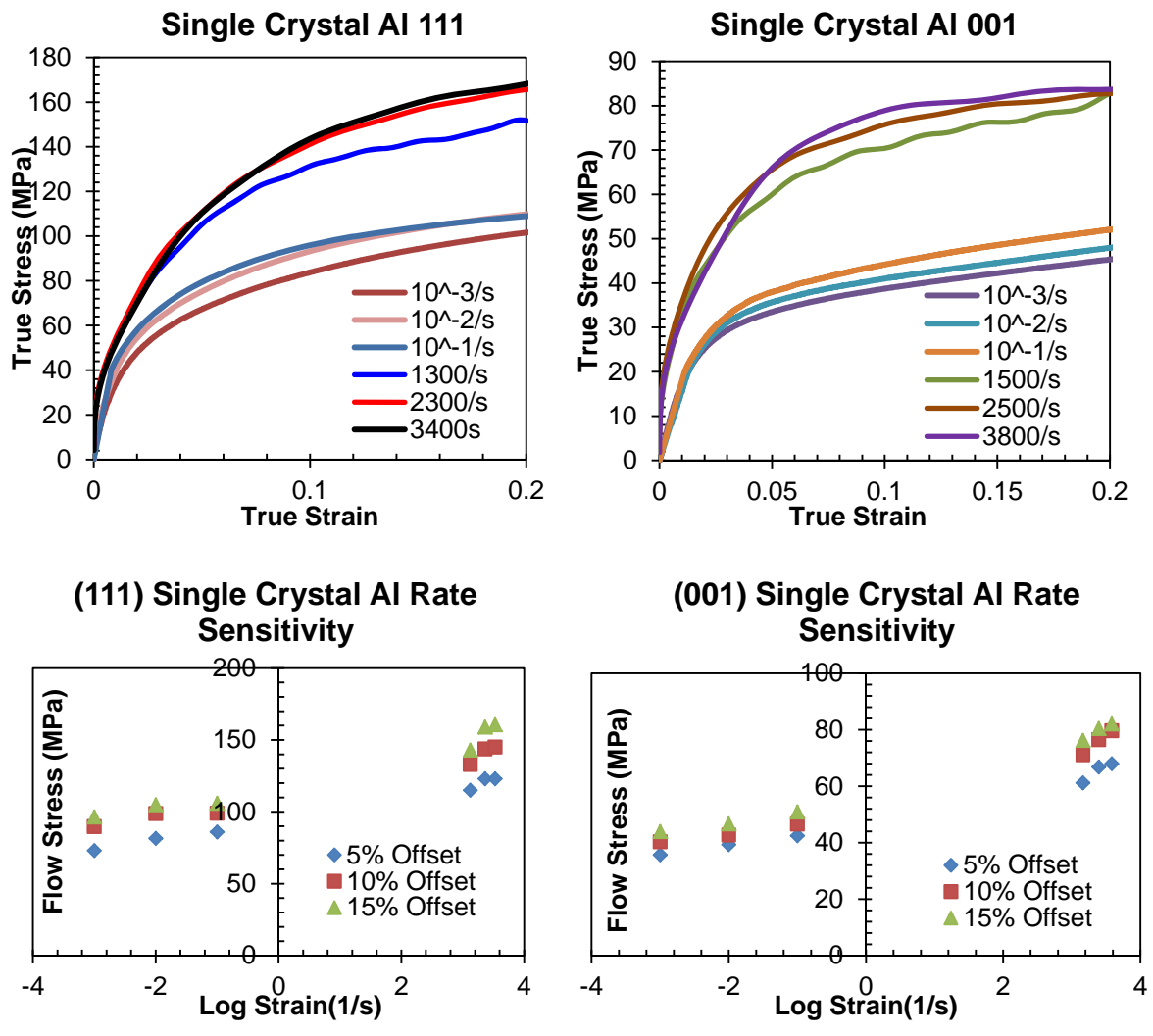


Figure 2.2. The material response of the two single crystals at quasi-static and dynamic regimes can be seen on the top row and the strain rate sensitivity of the two single crystals is presented at lower row. [Provided by H. Tran]

### 2.2 High-purity Polycrystalline Aluminum

After testing the single crystalline aluminum, the next step was testing polycrystalline aluminum material. As polycrystalline aluminum contains various grains in different orientations, the material strength would be somewhere in between the two single crystal aluminums (Fig. 2.3)

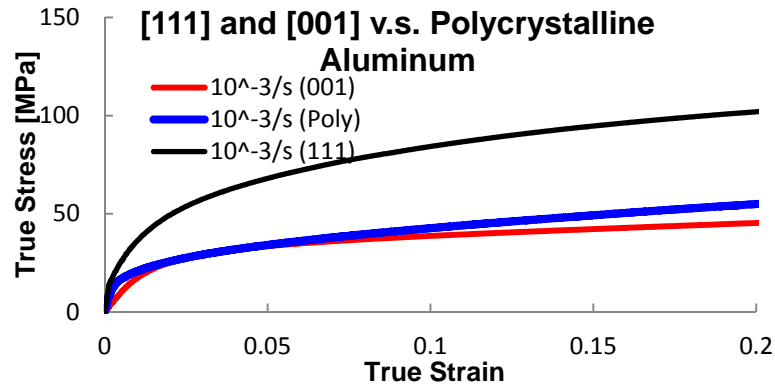


Figure 2.3. Comparison of the quasi-static performance of single crystalline and polycrystalline aluminum

Tests in quasi-static and dynamic regimes were conducted at room temperature and elevated temperatures (120° C and 220° C) (Fig. 3.5).

### 2.3 Solid Solution Aluminum Copper (0.1% Cu) Alloy

Next alloy is obtained by adding 0.1% (by weight) copper to the polycrystalline aluminum, which resulted in an aluminum alloy strengthened by solid solution of copper atoms. Flow stress values are very similar to that of polycrystalline aluminum (Fig 3.4).

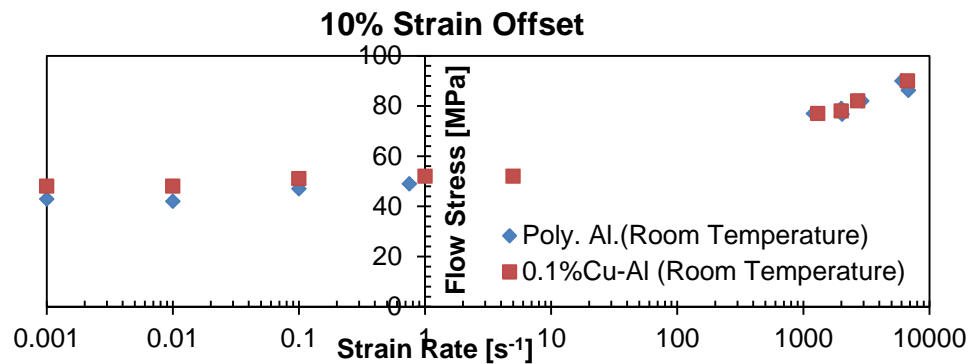


Figure 2.4. In quasi-static regime solid solution aluminum copper alloy display slightly higher flow stress values at 0.1 strain offset; while in dynamic regime both materials have very similar flow stress values ( Also similar trends in elevated temperatures).

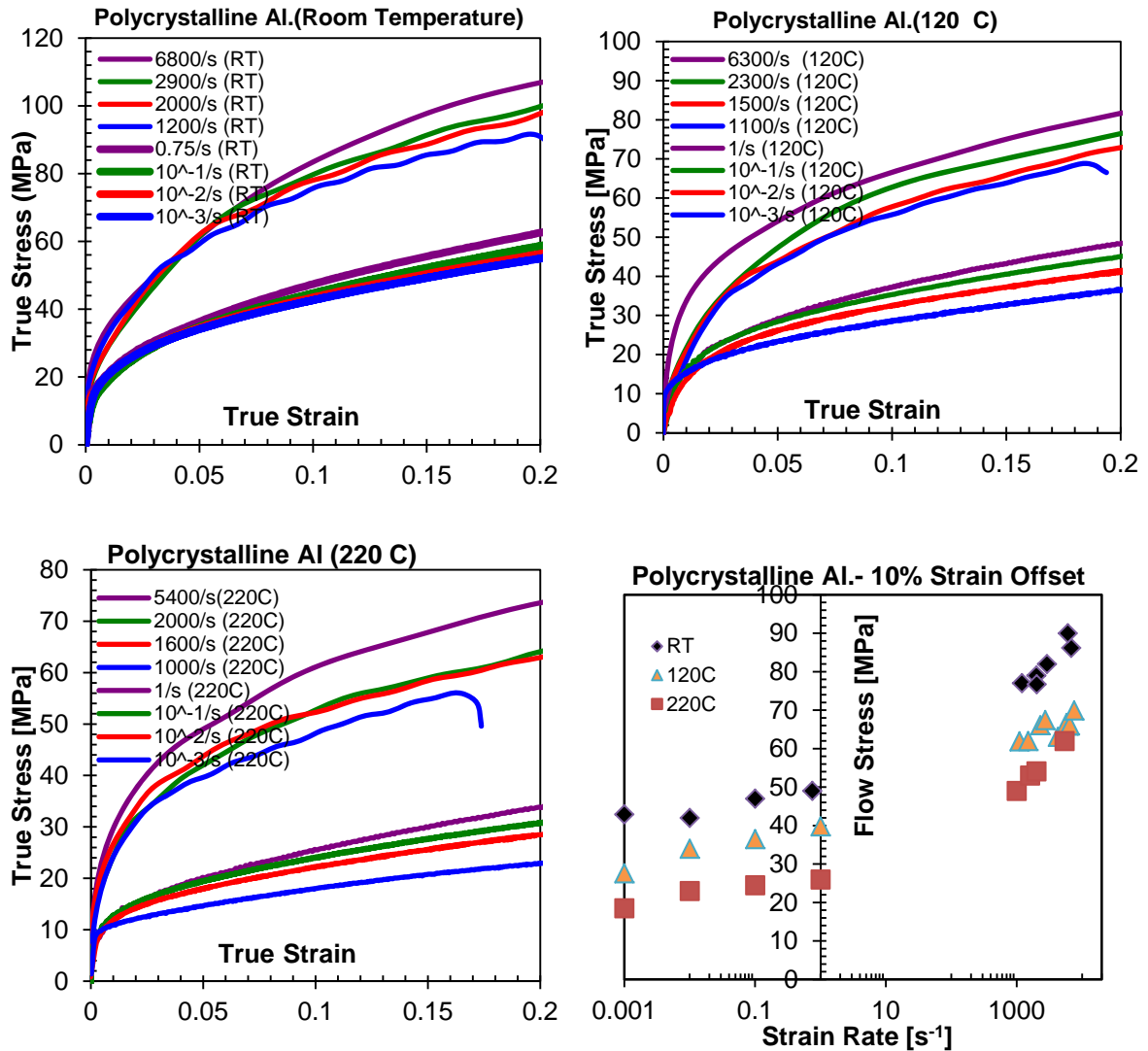


Figure 2.5. Top row and lower left graphs show the material response of polycrystalline aluminum in different temperatures. Lower right graph demonstrates the strain rate sensitivity of the material in these temperatures at 0.1 strain value.

To fully characterize the material, tests were done in quasi-static and dynamic regimes at room temperature and elevated temperatures (120° C and 220° C) (Fig. 3.6). Material response of polycrystalline aluminum and solid solution aluminum copper alloy are almost identical and they show increased rate sensitivity at the dynamic regime. Both materials also have increasing strain rate sensitivity with temperature in the quasi-static

regime. Room temperature flow stress values of these materials is much closer to [001] single crystalline aluminum than the [111] orientation.

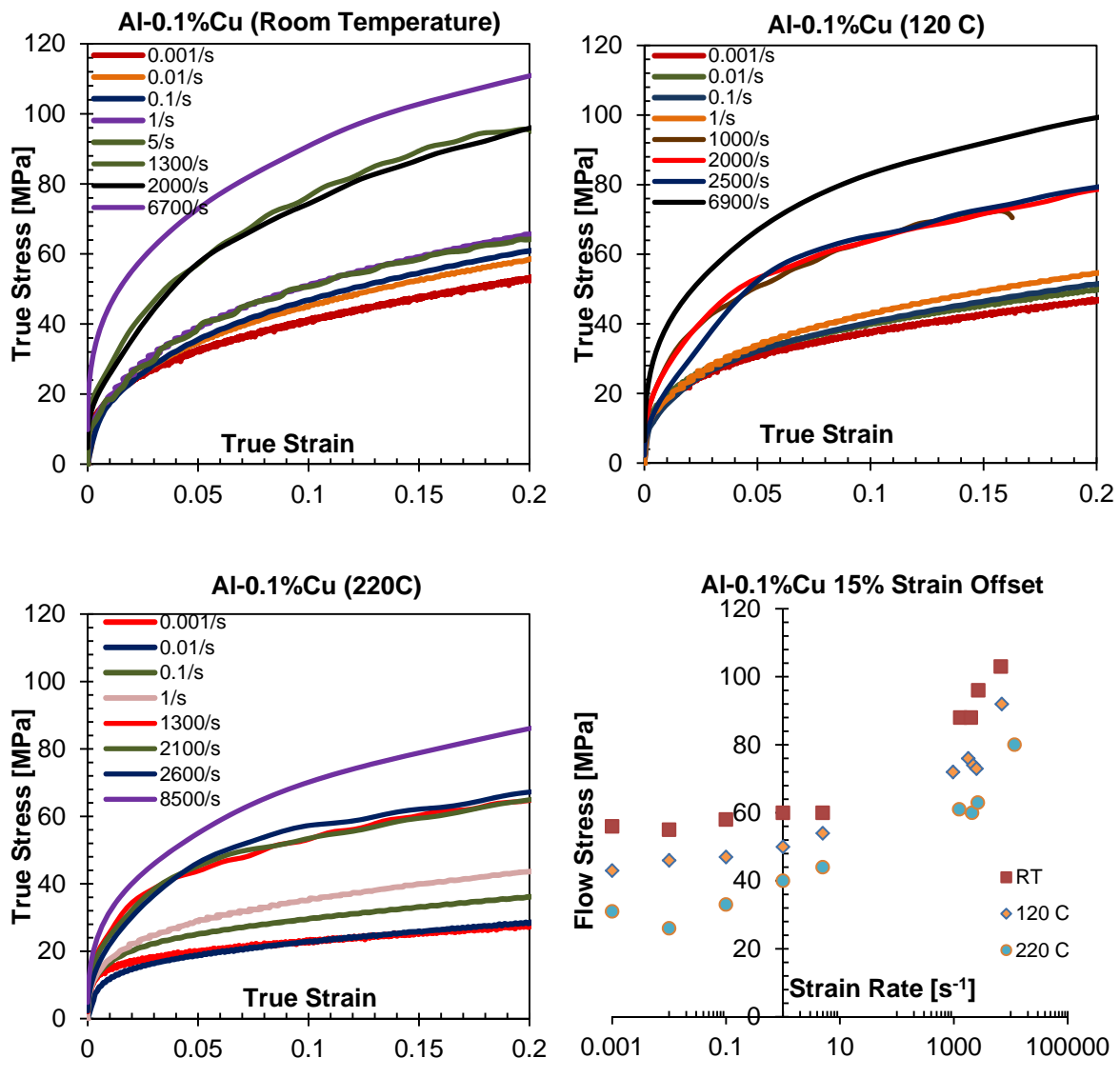


Figure 2.6. Top row and lower left graphs show the material response of solid solution aluminum copper alloy in different temperatures. Lower right graph demonstrates the strain rate sensitivity of the material in these temperatures at 0.1 strain offset value.

## 2.4 Al-4.5%Cu Alloy

With the addition of the 4.5% Cu, the new alloys start to become more microstructurally complex compared to the previous materials which do not contain any precipitations. Al-4.5%Cu alloy is the first alloy to have precipitations which are in the form of heterogeneous precipitation of  $\theta'$  phase. Compared to previous materials which have flow stress values less than 100 MPa, flow stresses jump to 400 MPa with the addition of precipitations. At this time only room temperature data is available for this alloy.

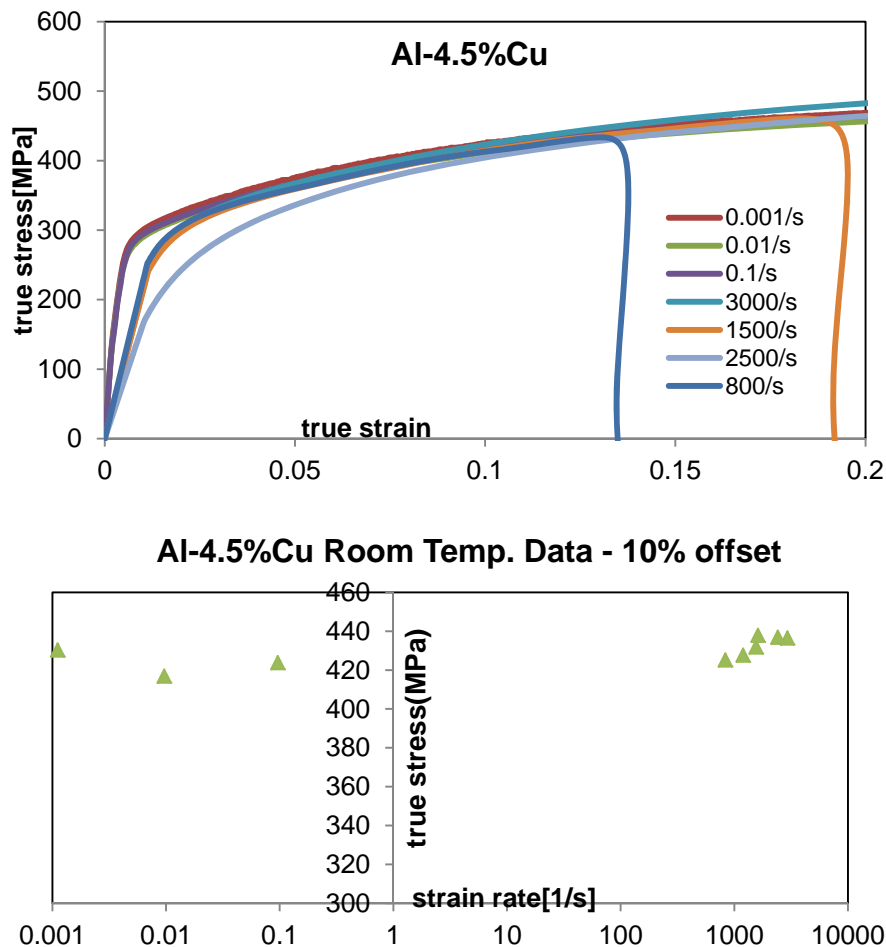


Figure 2.7. Room temperature experimental data for Al-4.5%Cu is shown. Since experiments are done till 3000/s strain rate, flow stress values are very similar in all experiments.

## 2.5 Al-4.5%Cu-0.5%Mg Alloy

The next alloy is obtained by adding 0.5%Mg (by weight) to the previous alloy.  $\theta'$  precipitations that were previously formed by the addition of the 4.5%Cu becomes more uniform with the addition of Mg and the new alloy comes out to be stronger than the Al-4.5%Cu alloy (Fig. 2.8).

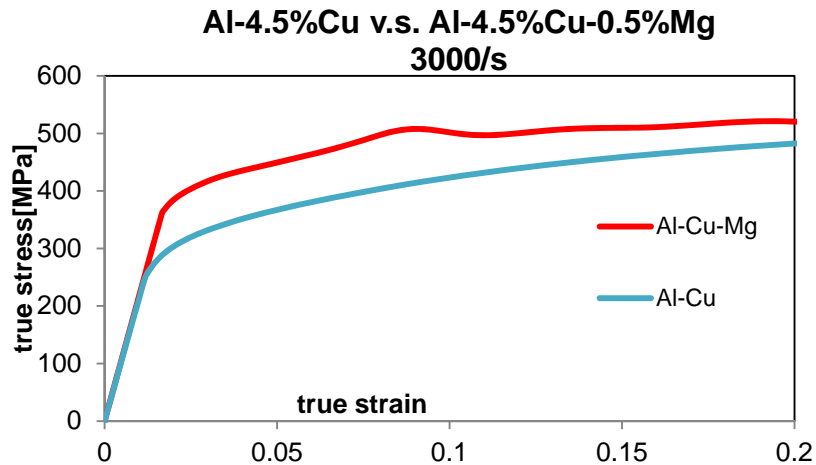


Figure 2.8. Comparison of Al-4.5%Cu and Al-4.5%Cu-0.5%Mg at the same strain rate. Addition of the Mg generates higher flow stress values.

At this point, only room temperature experimental data in quasi-static and dynamic regimes, and 220° C quasi-static regime experimental data is available (Fig. 2.9).

## 2.6 Al-4.5%Cu 0.5%Mg-0.3%Mn Alloy

Mn element (0.3% by weight) was added in this stage to the earlier Al-4.5%Cu-0.5%Mg alloy which resulted in  $Al_{20}Cu_2Mn_3$  dispersoids and  $\theta'$  precipitations to exist in this latest Al-4.5%Cu 0.5%Mg-0.3%Mn alloy. Flow stress is slightly higher compared to Al-4.5%Cu 0.5%Mg alloy (Fig 2.10).

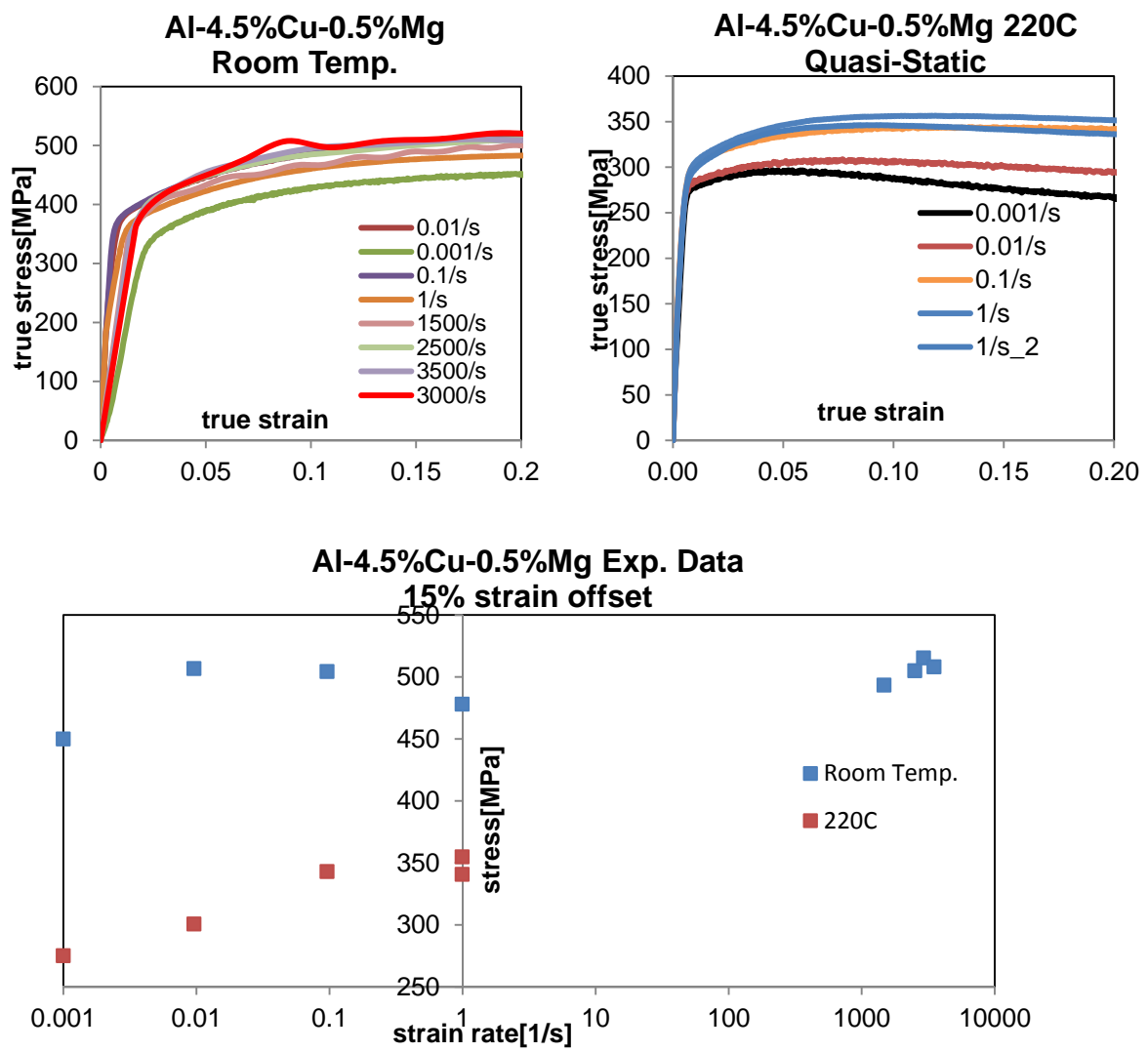


Figure 2.9. Current progress in Al-4.5%Cu-0.5%Mg alloy is presented. Since only strain rates up to 3000/s have been covered, flow stress values in dynamic regime are not very different from the quasi-static flow stress values. Only quasi-static data is available at 220° C.

Only room temperature experimental data is available for the Al-4.5%Cu 0.5%Mg-0.3%Mn alloy in the quasi-static and the dynamic regime (Fig.2.11).

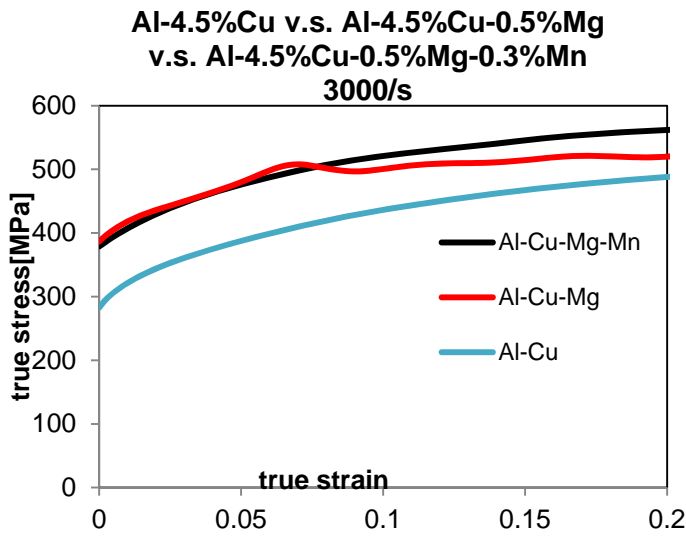


Figure 2.10. Comparison of the last three alloys in the dynamic regime. Al-4.5%Cu-0.5%Mg-0.3%Mn alloy has the highest flow stress values.

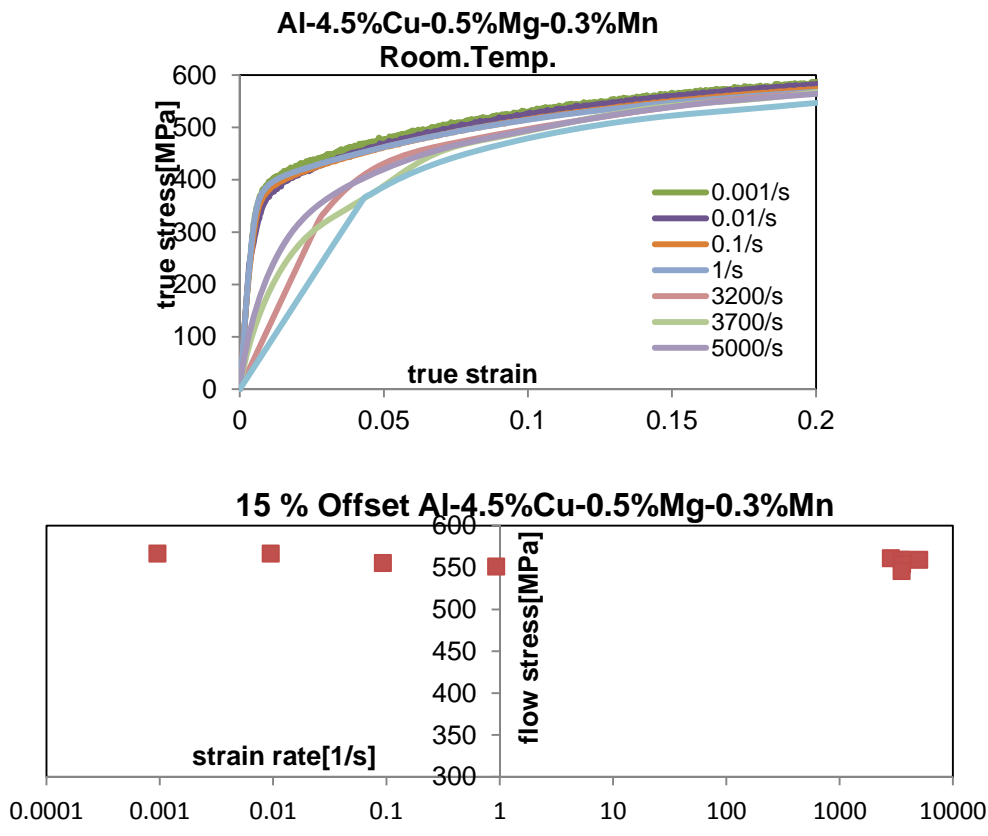


Figure 2.11. Room temperature data for the A-4.5%Cu-0.5%Mg-0.3%Mn alloy is presented.

## 2.7 Al-4.5%Cu 0.5%Mg-0.3%Mn -0.3%Ag Alloy

The most complex alloy was obtained with the addition of Ag element which resulted in  $\Omega$  precipitations,  $\text{Al}_{20}\text{Cu}_2\text{Mn}_3$  dispersoids and  $\theta'$  precipitations. Dynamic and quasi-static tests were conducted at room temperature and 220°C. Also 0.001/s quasi-static tests were done at elevated temperatures to capture thermal softening behavior.

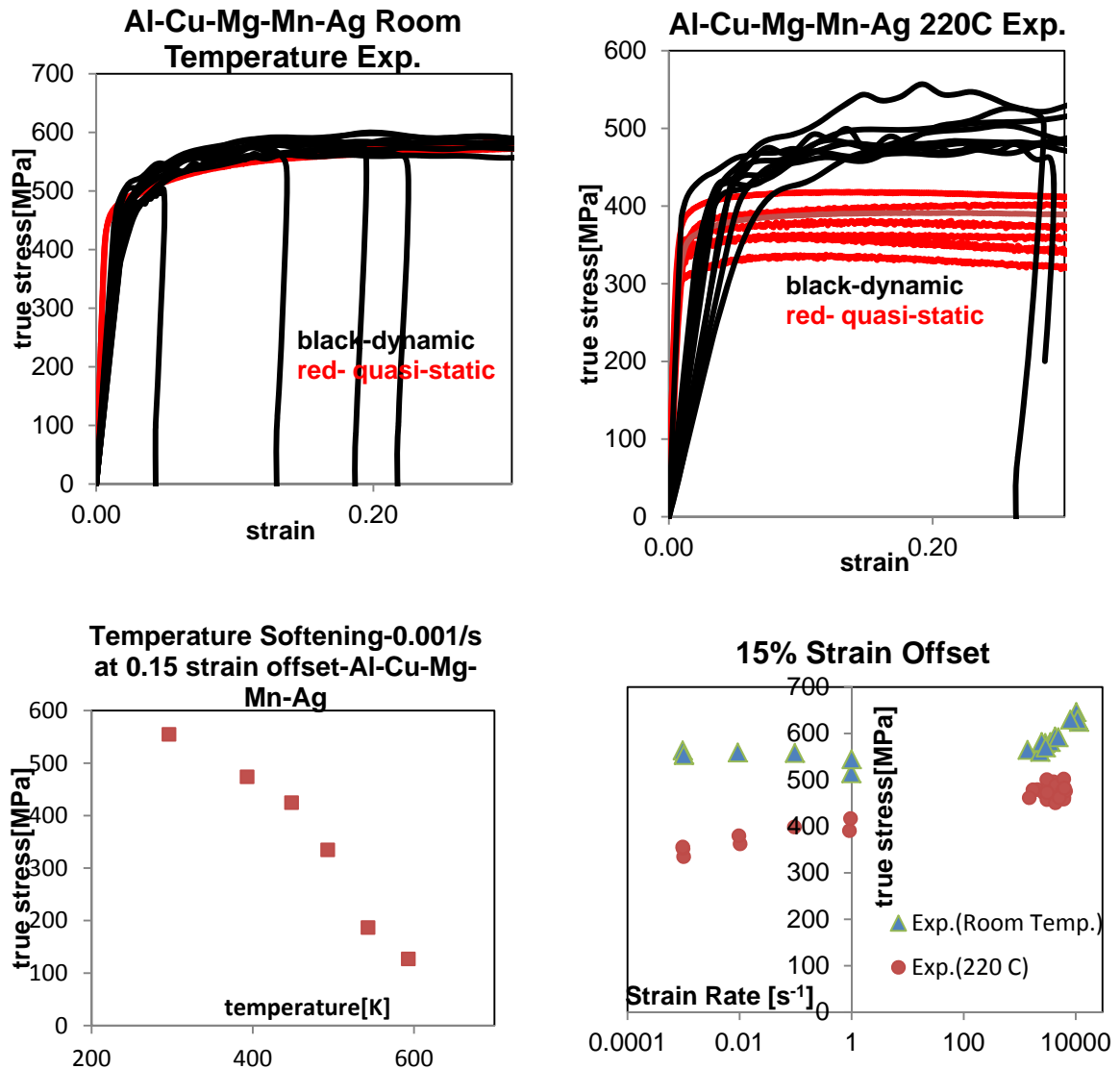


Figure 2.12. Room temperature and 220°C experimental data are presented at the upper row. Lower left graph show the thermal softening behavior. Lower right graph show all the experimental data in 0.15 strain offset.

Al-4.5%Cu 0.5%Mg-0.3%Mn -0.3%Ag alloy has the highest flow stress values among the alloys that were tested (Fig. 2.13).

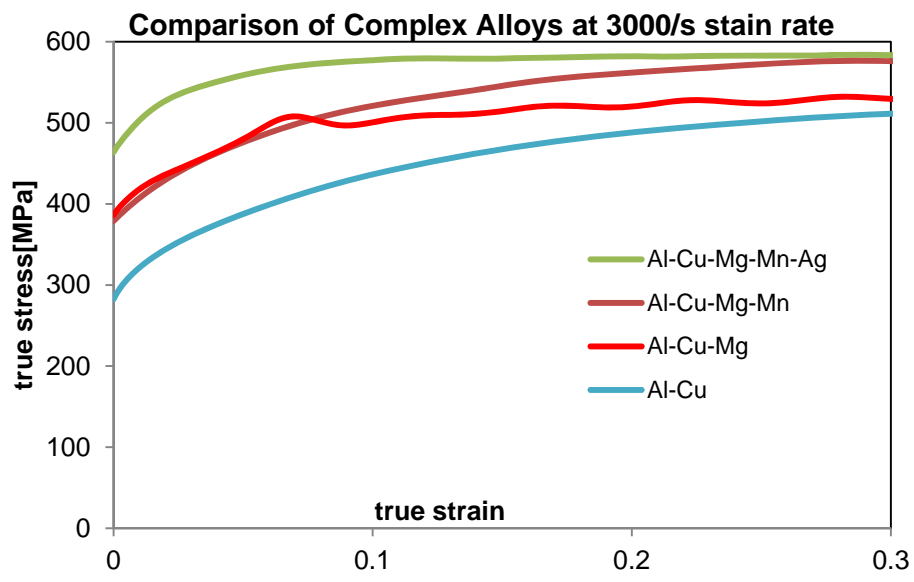


Figure 2.13. Al-4.5%Cu 0.5%Mg-0.3%Mn -0.3%Ag alloy has the highest flow stress values among the other complex alloys. However after 0.3 strain, Al-4.5%Cu 0.5%Mg-0.3%Mn reaches the same flow stress value with the Ag alloy.

## CHAPTER 3

## MODIFIED ZERILLI-ARMSTRONG MODEL

**3.1 Introduction**

Although Modified Johnson-Cook model excels at capturing material behavior, but it has no physical roots. MTS model seems as an ideal candidate for this task, but it has its shortcomings. Since MTS model employs threshold stress to model the structure, first threshold stress should be modeled. To model evolution of threshold stress with strain rate and temperature, stress jump tests must be conducted (Follansbee, Kocks and Regazzoni 1985). After each dynamic test with stop rings, the specimens must be reshaped as soon as possible to conduct quasi-static tests without any room temperature annealing. Therefore it would take considerably more time to complete tests required for MTS model compared to regular tests required for other material models. Meanwhile it has more than fifteen parameters, which makes it challenging to fit all parameters computationally without in advance assuming values in some of the parameters.

Even though ZA model is considerably simpler than the MTS model, it is not possible to model the aluminum-copper alloys due to its hardening term. ZA model has a hardening term of  $B_0 \varepsilon^{\frac{1}{2}} e^{-\alpha T}$ , thus flow stress is proportional to square root of the strain; while aluminum-copper alloys show saturation behavior after some point(Fig 3.1). But hardening parameter can be modified to show saturation stress.

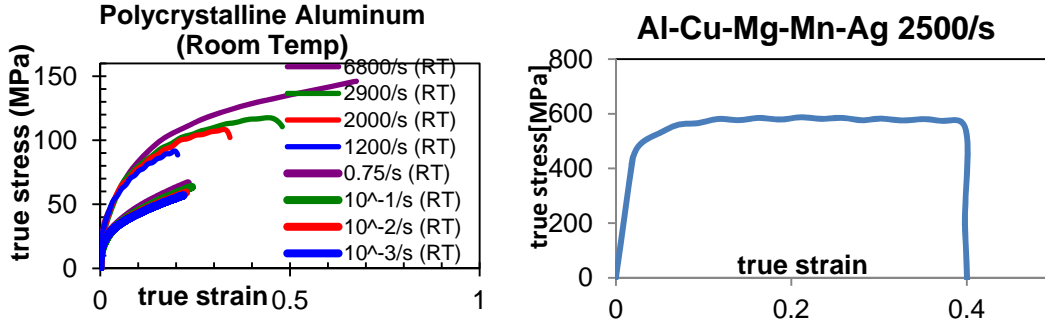


Figure 3.1. Polycrystalline aluminum shows hardening behavior akin to ZA model's hardening parameter, whereas aluminum-copper alloys show decreasing hardening rate with increasing strain rate.

If original Zerilli-Armstrong model is used to model the Al-Cu-Mg-Mn-Ag alloy, it is not possible to capture the increased rate sensitivity after 1000/s strain rate in the dynamic regime and also the error between the model and the experimental data grows with increasing strain which indicates a different strain hardening behavior than the ZA model (fig. 3.2).

### 3.2 Former Modifications to ZA Model by Zerilli and Armstrong

To overcome the difficulty of modeling materials that show saturation behavior, Zerilli and Armstrong modified the ZA model to include dynamic recovery process (Zerilli and Armstrong 1997). The mechanical strength of obstacles to dislocation glide,  $\hat{\sigma}$ , the threshold stress, is related to dislocation density :

$$\hat{\sigma} = \alpha \mu b \rho^{\frac{1}{2}} \quad (3.1)$$

Therefore dislocation density can be used to model the threshold stress. Heuristically, the density of the immobile dislocations may be related to the strain by:

$$\frac{d\rho_i}{d\varepsilon} = \frac{1}{b\lambda} - \omega\rho_i \quad (3.2)$$

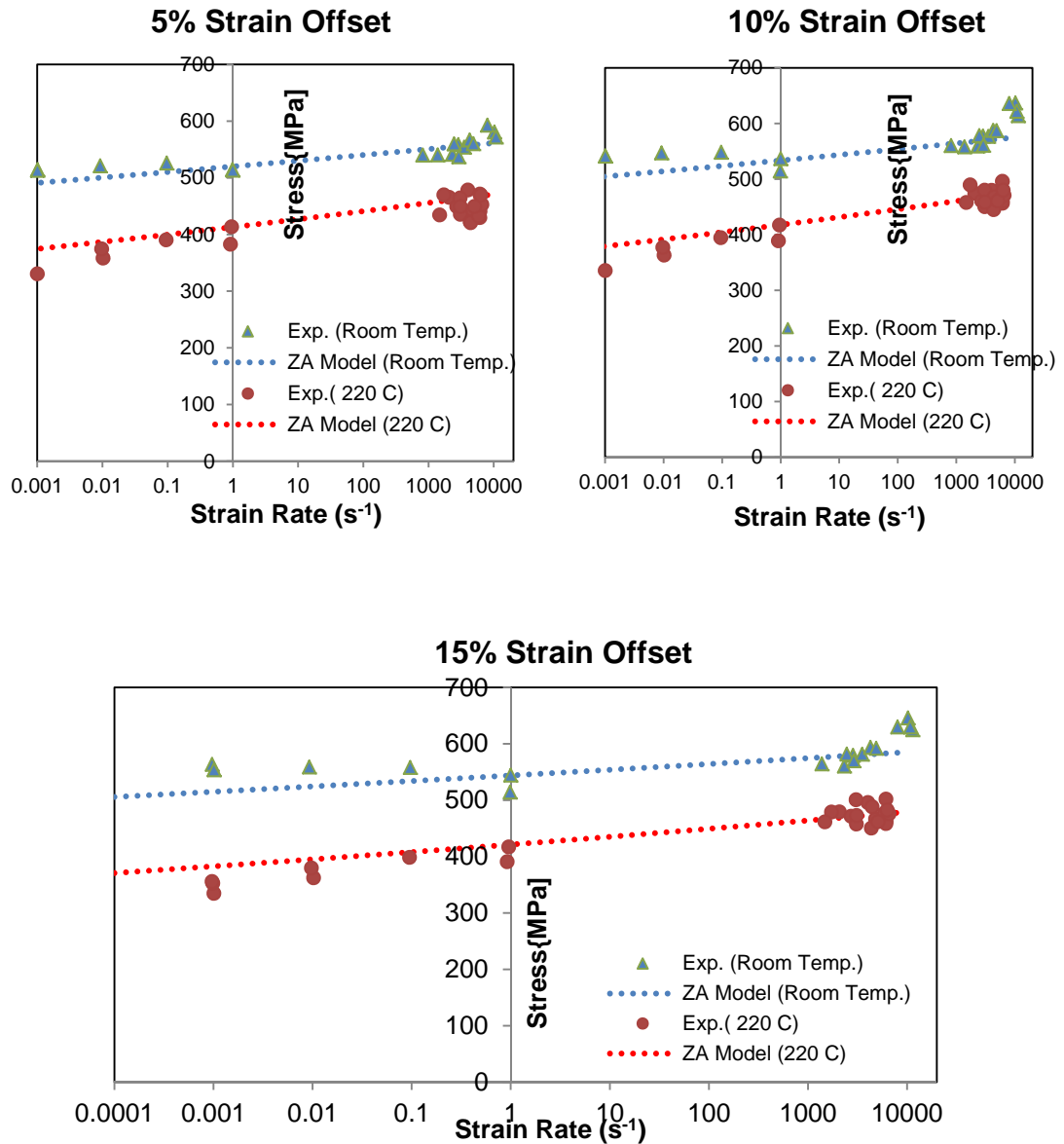


Figure 3.2. Original Zerilli-Armstrong Model is used to model the Al-Cu-Mg-Mn-Ag alloy. Model fails to capture the increased strain-rate sensitivity in the dynamic regime.

where  $\lambda$  is the mean free path for immobilization of mobile dislocations and  $\omega$  is the probability for remobilizing or annihilating a stopped dislocation. Eq. 3.2 can be integrated to find the relation between strain and dislocation density:

$$\frac{d\rho}{\frac{1}{\lambda b} - \omega\rho} = d\varepsilon$$

$$\int \frac{d\rho}{\frac{1}{\lambda b} - \omega\rho} = \int d\varepsilon \quad (3.3)$$

$$\frac{1}{\omega} \ln(1 - \lambda b \omega \rho) = -\varepsilon$$

By merging Eq.3.3 with Eq. 3.1, an expression for the threshold stress can be found:

$$\hat{\sigma} = \alpha\mu \sqrt{\frac{b}{\lambda}} \sqrt{\frac{1}{\omega} (1 - e^{-\omega\varepsilon})} \quad (3.4)$$

With this new definition of the threshold stress, the thermal component of the ZA model becomes:

$$\sigma_{th} = B e^{-\beta T} + \left[ \alpha\mu \sqrt{\frac{b}{\lambda}} \sqrt{\frac{1}{\omega} (1 - e^{-\omega\varepsilon})} \right] e^{-\alpha T} \quad (3.5)$$

where

$$\alpha = \alpha_0 - \alpha_1 \ln(\dot{\varepsilon})$$

$$\beta = \beta_0 - \beta_1 \ln(\dot{\varepsilon}) \quad (3.6)$$

A different problem with the ZA model in modeling aluminum-copper alloys is capturing the increased strain rate sensitivity of these alloys in the dynamic regime. Zerilli and Armstrong again modified the thermal component of ZA model to include this strain rate sensitivity effect in the dynamic region:

$$\sigma^* = 0.5\sigma_{th} \left[ 1 + \left( 1 + \frac{4c_0\dot{\varepsilon}T}{\sigma_{th}} \right)^{\frac{1}{2}} \right] \quad (3.7)$$

where  $c_0$  is a constant in the order of  $10^{-5}$  MPa/K. In the quasi-static regime,  $\frac{4c_0\dot{\epsilon}T}{\sigma_{th}}$  term will be very small and negligible, and therefore  $\sigma^*$  will be almost equal to  $\sigma_{th}$ . However, as  $\frac{4c_0\dot{\epsilon}T}{\sigma_{th}}$  term gets bigger and bigger in the dynamic region, the ZA model will show the desired increased rate sensitivity in the dynamic region.

### 3.3 Modifications to ZA Model

With the entire modifications ZA model become (Modified Zerilli-Armstrong Model):

$$\begin{aligned}\sigma &= \sigma_a + \sigma^* \\ \sigma^* &= 0.5\sigma_{th} \left[ 1 + \left( 1 + \frac{4c_0\dot{\epsilon}T}{\sigma_{th}} \right)^{\frac{1}{2}} \right] \\ \sigma_{th} &= B e^{-\beta T} + \left[ \alpha \mu \sqrt{\frac{b}{\lambda}} \sqrt{\frac{1}{\omega} (1 - e^{-\omega \epsilon})} \right] e^{-\alpha T}\end{aligned}\tag{3.8}$$

where

$$\begin{aligned}\alpha &= \alpha_0 - \alpha_1 \ln(\dot{\epsilon}) \\ \beta &= \beta_0 - \beta_1 \ln(\dot{\epsilon})\end{aligned}\tag{3.9}$$

With these modifications to the MZA Model, the model finally can capture the increased strain-rate sensitivity in the dynamic regime. As Figure 3.3 illustrates, the MZA model can accurately capture the experimental data in quasi-static and dynamic regimes at room temperature and 220° C. Although the equations seem to work pretty well, the problem is with the elevated temperatures. Flow stress is associated to the temperature in an exponential manner which gives unrealistic results after some point (Fig 3.4). To accurately capture the experimental data in a greater temperature range, the exponential

relation between the flow stress and the temperature must be altered. Only way to modify this relation is to make one of the constants temperature dependent. Constants  $\alpha, \mu, b$  are more or less constant with temperature, and the term B cannot be assumed to decrease with temperature as there is not any physical basis.

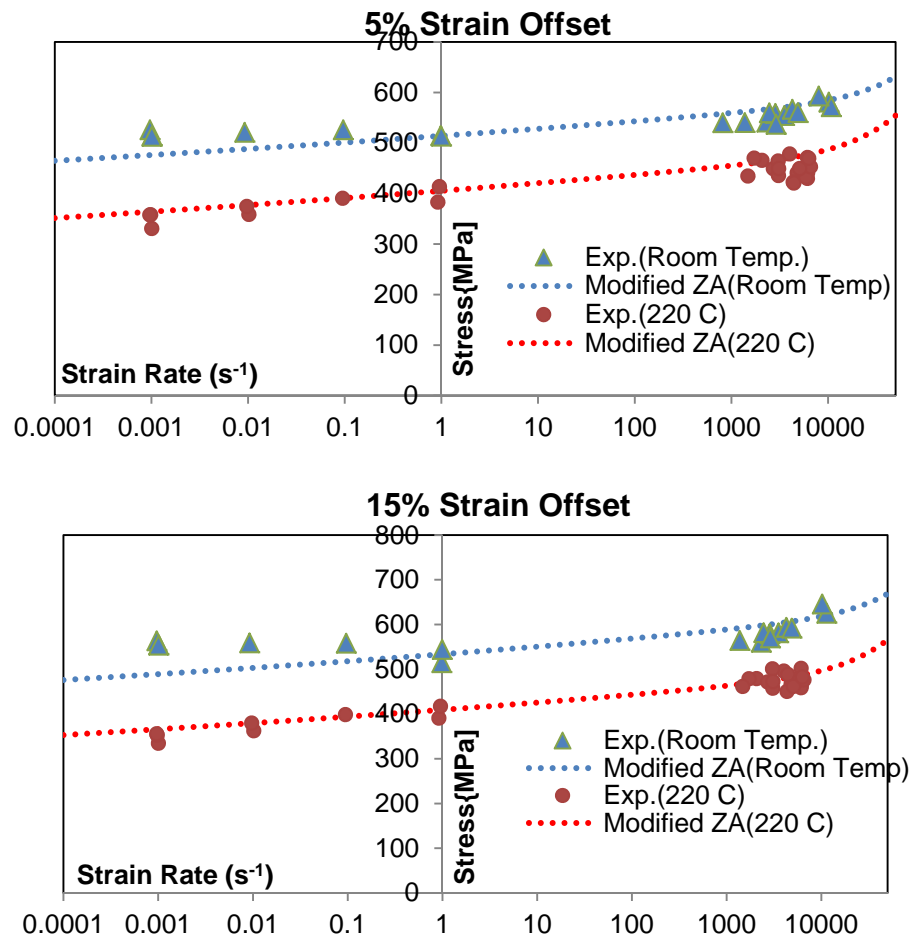


Figure 3.3. Al-Cu-Mg-Mn-Ag alloy modeled with Modified Zerilli-Armstrong Model which shows increased strain-rate sensitivity in the dynamic regime.

Neither of the two physical material models (MTS and ZA models) takes account of the effect of the diffusion process on the threshold stress. With the help of the diffusion, dislocations can overcome the barriers by leaving their planes.

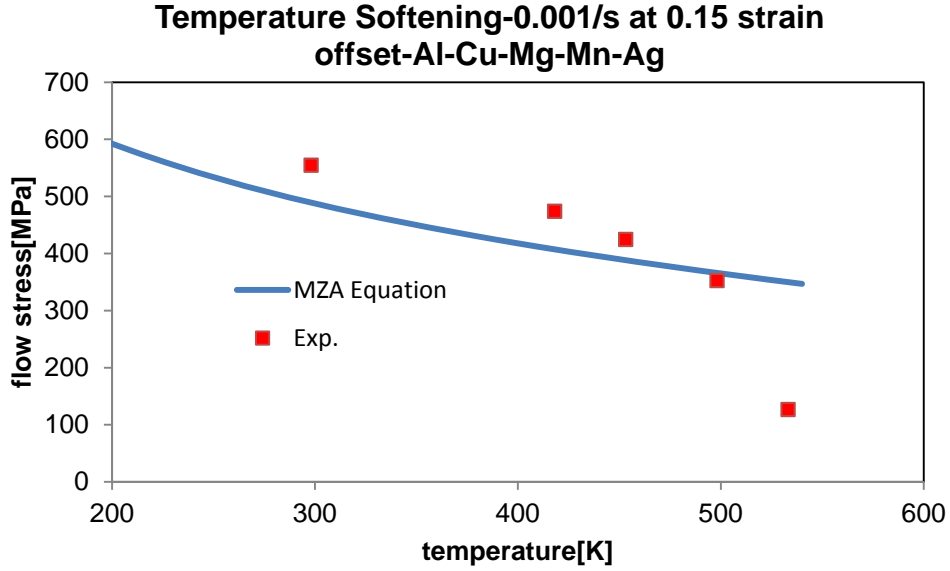


Figure 3.4. Thermal softening of the flow stress is shown. After 500K, model behavior is very dissimilar to the experimental results.

Mean free path for immobilization of mobile dislocations ( $\lambda$ ) will be affected by this process by getting larger with increasing temperature. Thus thermal component can be modified as:

$$\sigma_{th} = \left[ \alpha \mu \sqrt{\frac{b}{\lambda(T)}} \sqrt{\frac{1}{\omega} (1 - e^{-\omega \varepsilon})} \right] e^{-\alpha T} + B e^{-\beta T} \quad (3.10)$$

$$\sigma_{th} = \left[ A(T) \sqrt{\frac{1}{\omega} (1 - e^{-\omega \varepsilon})} \right] e^{-\alpha T} + B e^{-\beta T}$$

where  $A(T)$  is a material specific temperature dependent constant which decreases with increasing temperature. Also if  $B e^{-\beta T}$  term is removed, thermal stress becomes:

$$\sigma_{th} = \left[ A(T) \left( 1 + \sqrt{\left( \frac{1}{\omega} (1 - e^{-\omega \varepsilon}) \right)} \right) \right] e^{-\alpha T} \quad (3.11)$$

With this modification,  $Be^{-\beta T}$  term can be removed since  $A(T)e^{-\alpha T}$  component of the new thermal stress will work same as the latter, and also with this modification threshold stress becomes analogous to threshold stress definition in MTS model (Eq. 1.49 and Eq. 1.50), where threshold stress has strain dependent and independent components. Furthermore by removing this term, the new model will have three less parameters ( $\beta_1, \beta_2,$  and B) without any loss in functionality and deviation from dislocation physics. Considering all modifications, Turkkan-Vural Modified Zerilli-Armstrong (TVZA) model turn into:

$$\begin{aligned}\sigma &= \sigma_a + \sigma^* \\ \sigma^* &= 0.5\sigma_{th} \left[ 1 + \left( 1 + \frac{4c_0\dot{\epsilon}T}{\sigma_{th}} \right)^{\frac{1}{2}} \right] \\ \sigma_{th} &= \left[ A(T) \left( 1 + \sqrt{\left( \frac{1}{\omega} (1 - e^{-\omega\epsilon}) \right)} \right) \right] e^{-\alpha T}\end{aligned}\tag{3.12}$$

where

$$\begin{aligned}\alpha &= \alpha_0 - \alpha_1 \ln(\dot{\epsilon}) \\ A(T) &= A \left( 1 - \left( \frac{T - T_0}{T_m - T_0} \right)^p \right)\end{aligned}\tag{3.13}$$

After these modifications, ZA model can finally capture the material behavior of Al-Cu alloys at high temperatures and  $A(T)$  can be modified to capture the desired thermal softening behavior of other different materials (Fig. 3.5). Similar to the MZA Model which was effective at capturing the experimental data at relatively low temperatures,

TVZA model can accurately capture the experimental data at room temperature and 220°

C.

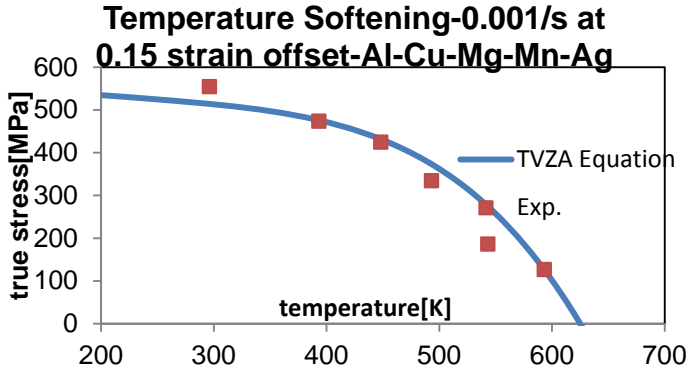


Figure 3.5. TVZA model can successfully capture the softening behavior of the alloy even at temperatures above 500 K.

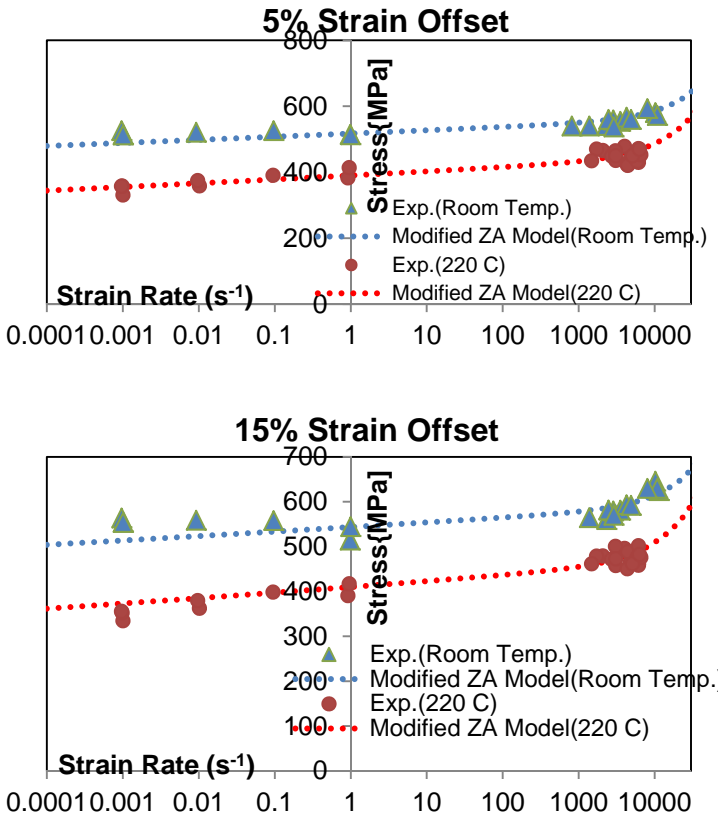


Figure 3.6. Al-Cu-Mg-Mn-Ag alloy modeled with Turkkan-Vural Modified Zerilli-Armstrong Model which shows increased strain-rate sensitivity in the dynamic regime.

## CHAPTER 4

## MODELING THE EXPERIMENTAL DATA

**4.1 Introduction**

Al-4.5%Cu, Al-4.5%Cu-0.5%Mg, and Al-4.5%Cu-0.5%Mg-0.5%Mn alloys have only room temperature data, but the rest of the materials have room temperature and elevated temperature experimental data in quasi-static and dynamic regimes. Therefore the following alloys which have complete set of experimental data were modeled in this chapter:

- [100] and [111] Single Crystals
- Polycrystalline Al.
- Al-0.1%Cu.
- Al-4.5%Cu-0.5%Mg-0.3%Mn-0.3%Ag

As discussed in Chapter 3, original Zerilli-Armstrong Model excels in capturing less complex alloys such as Single Crystal Aluminum, Polycrystalline Aluminum and Al-0.1%Cu. Therefore these materials were modeled using the original ZA model with only increased rate sensitivity modification (Eq. 3.7).

$$\sigma = \sigma_a + \sigma^*$$

$$\sigma^* = 0.5\sigma_{th} \left[ 1 + \left( 1 + \frac{4c_0\dot{\epsilon}T}{\sigma_{th}} \right)^{\frac{1}{2}} \right]$$

$$\sigma_{th} = B_0\epsilon^{\frac{1}{2}}e^{-\alpha T}$$
(4.1)

where

$$\alpha = \alpha_0 - \alpha_1 \ln(\dot{\epsilon}) \quad (4.2)$$

Al-4.5%Cu-0.5%Mg-0.3%Mn-0.3%Ag alloy was modeled using the Turkkan-Vural Modified Zerilli-Armstrong Model. Moreover, the listed alloys were modeled using Modified Johnson-Cook Model.

#### 4.2 [100] and [111] Single Crystals

Single Crystalline Aluminum has only room temperature data and no further experiments will be conducted at elevated temperatures. Therefore, Single Crystalline Aluminum was modeled using only original ZA Model (Fig. 4.1) (Fig. 4.2).

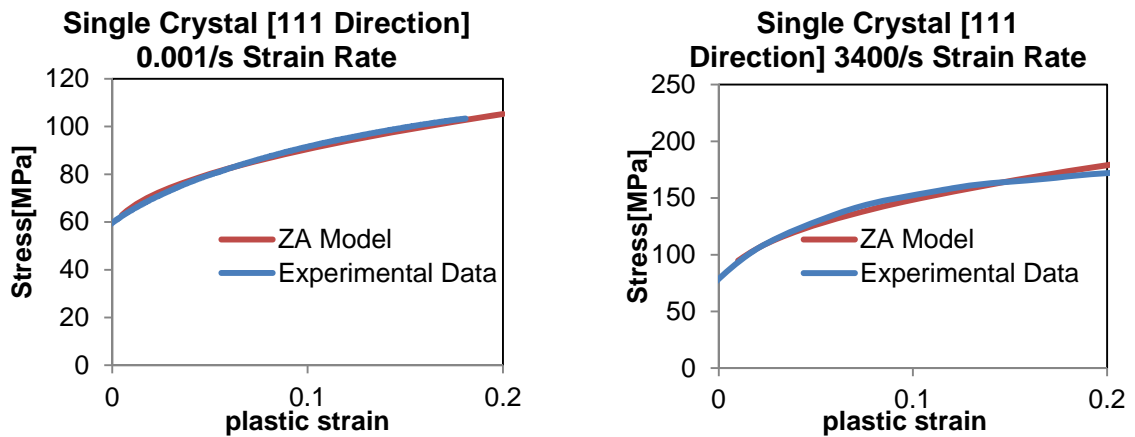


Figure 4.1. Single Crystalline [111] direction aluminum modeled with original ZA Model.

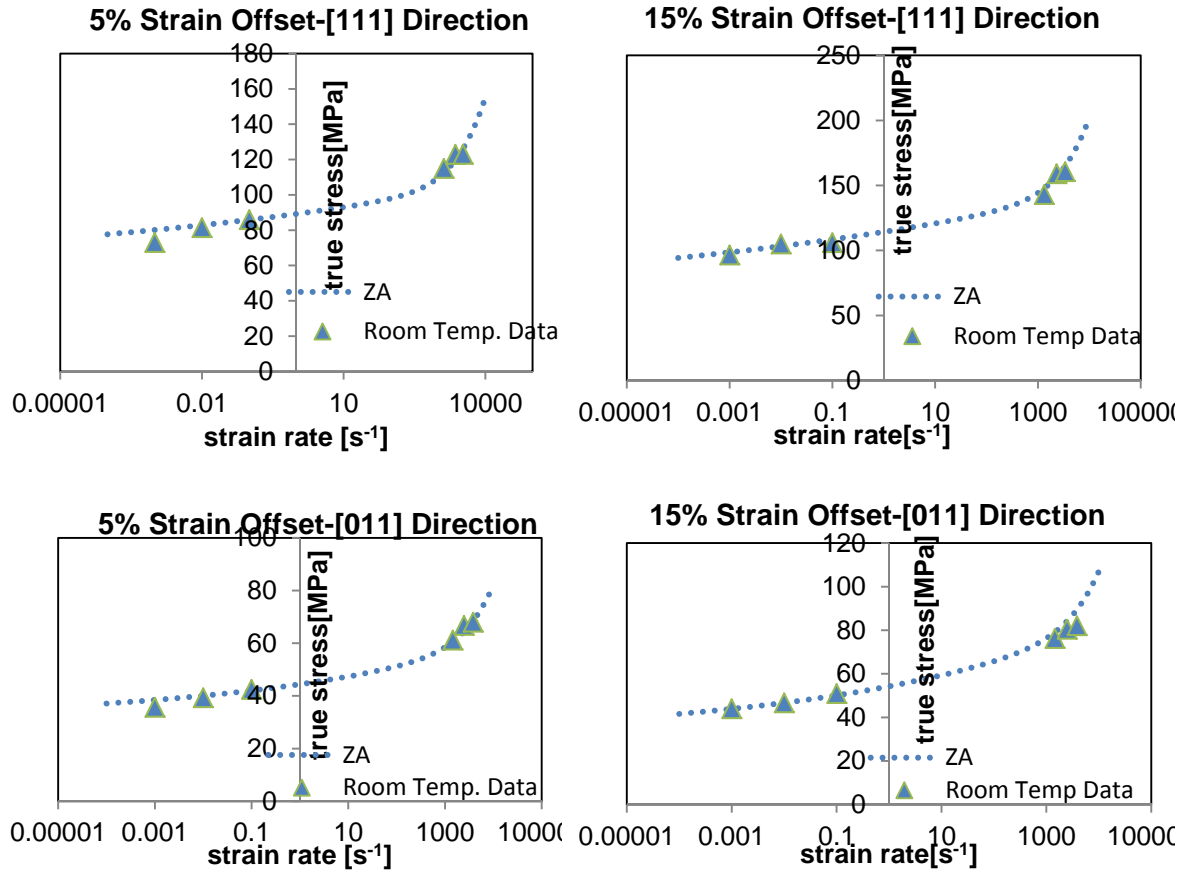


Figure 4.2. Single Crystalline [111] and [011] direction aluminum modeled with original ZA Model.

### 4.3 Polycrystalline Aluminum

Polycrystalline Aluminum have complete set of experiments in room temperature, 120° C ,and 220° C. Modified Johnson-Cook Model and Zerilli-Armstrong Model were used to model the experimental data.

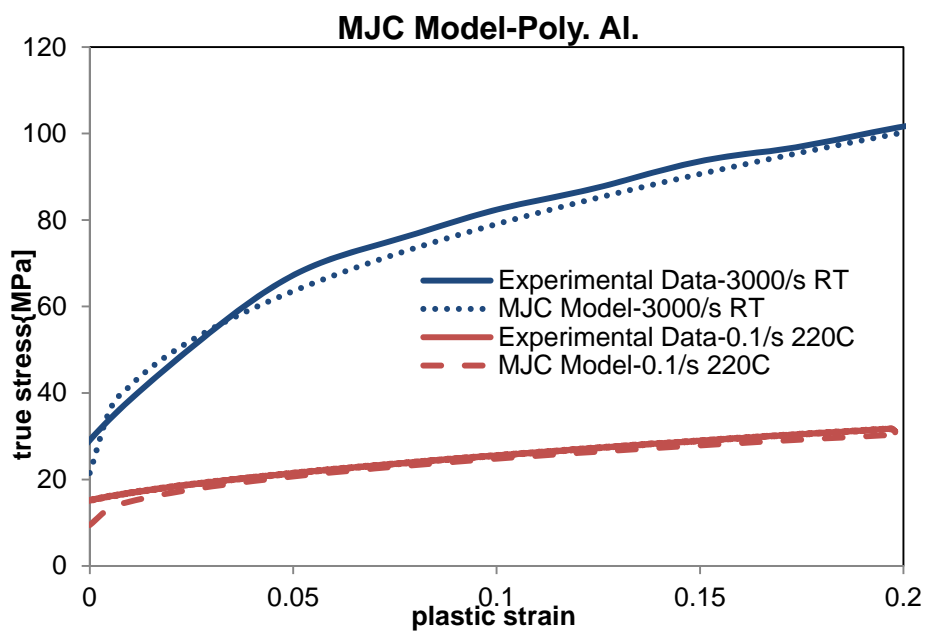
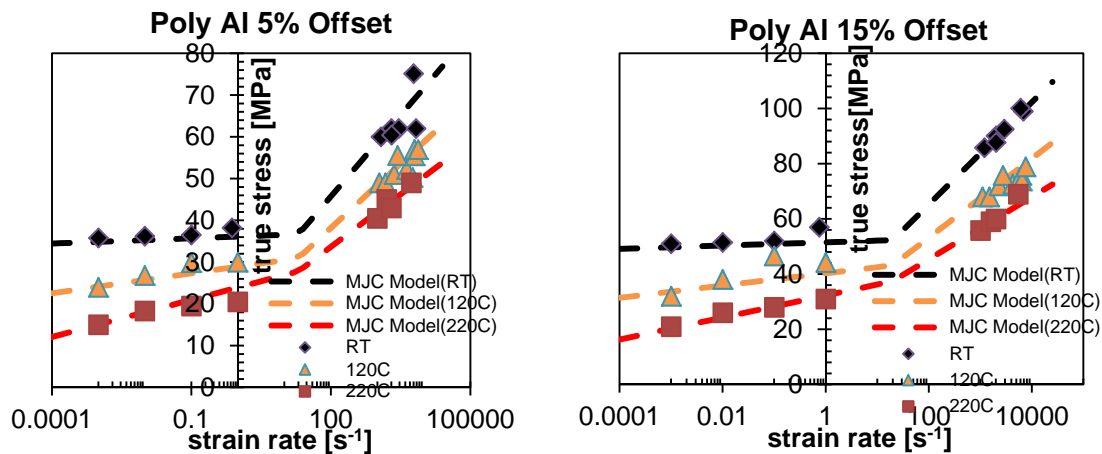


Figure 4.3. Polycrystalline aluminum modeled with MJC Model.

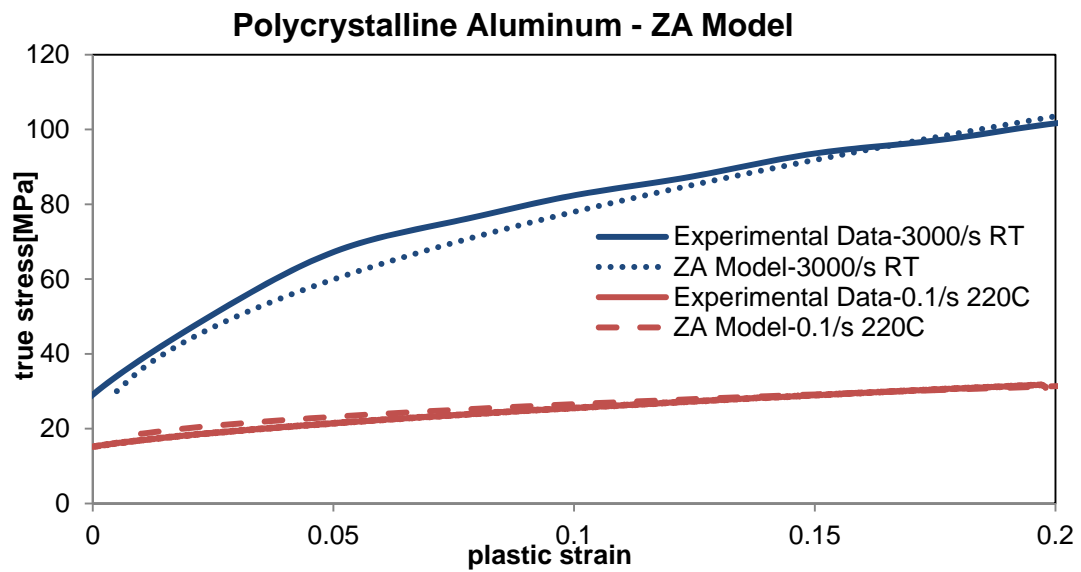
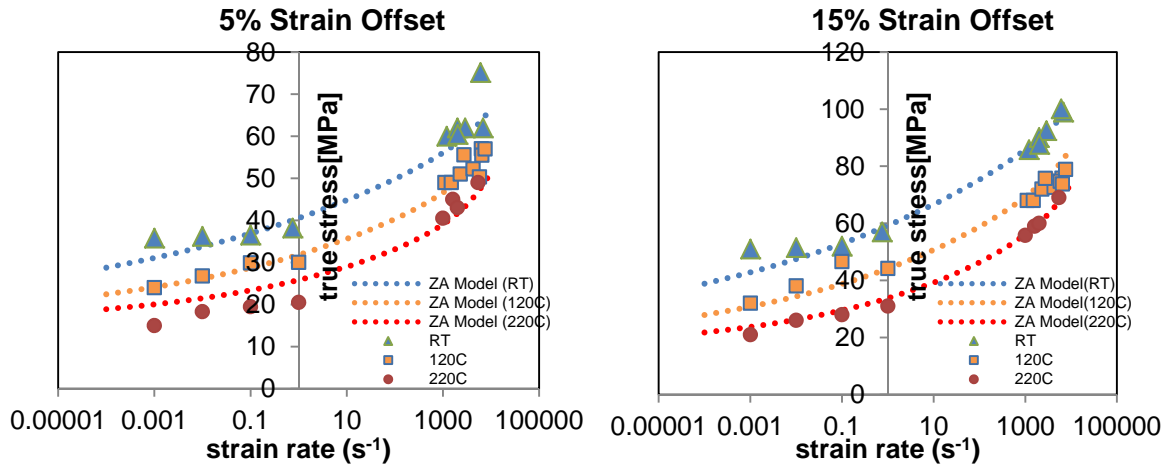


Figure 4.4. Polycrystalline aluminum modeled with ZA Model.

#### 4.4 Al-0.1%Cu Alloy

Al-0.1%Cu alloy have complete set of experiments in room temperature, 120° C ,and 220° C. Modified Johnson-Cook Model and Zerilli-Armstrong Model were used to model the experimental data (Fig 4.5)(Fig. 4.6).

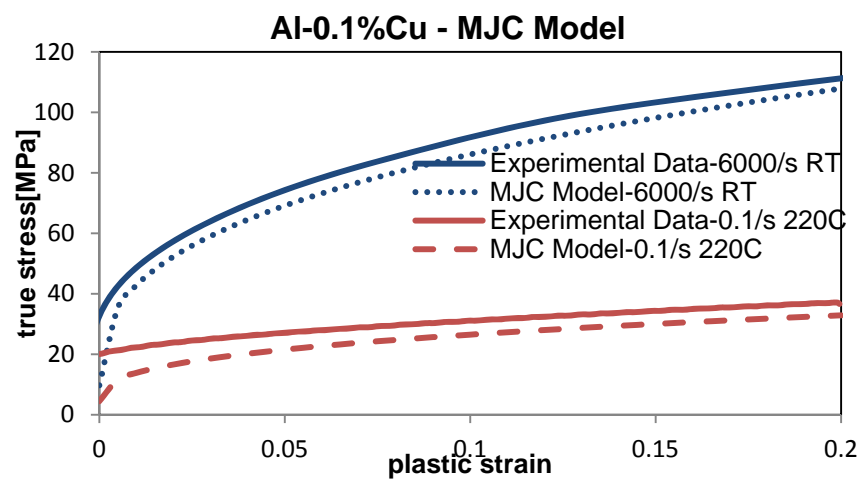
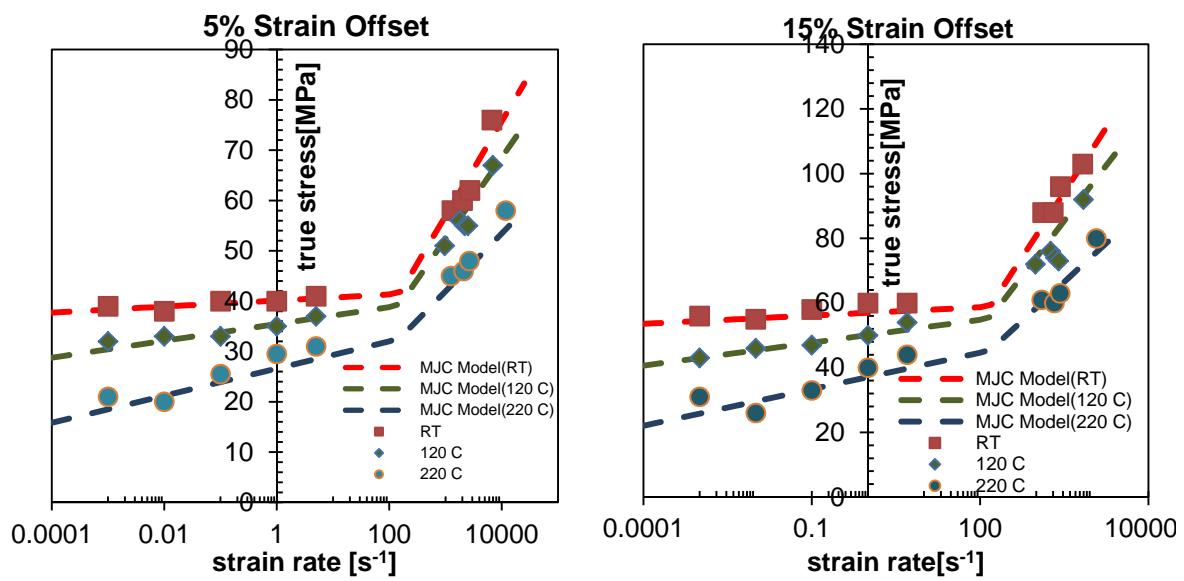


Figure 4.5. Al-0.1%Cu modeled with MJC Model

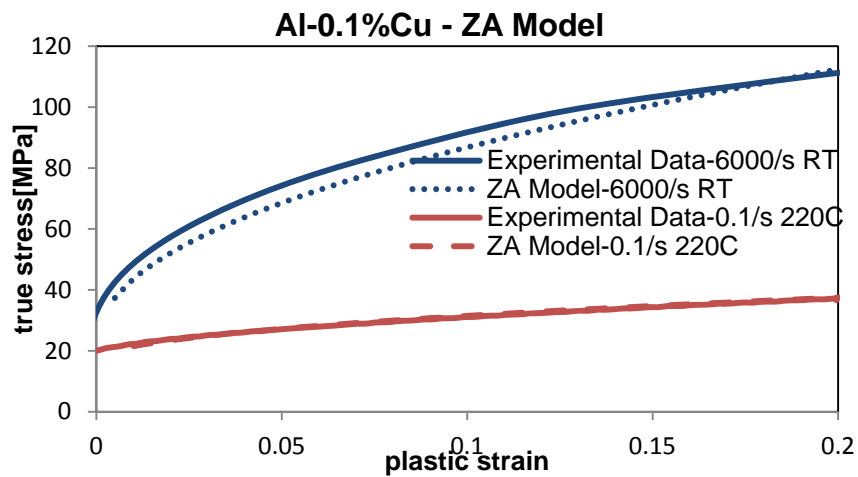
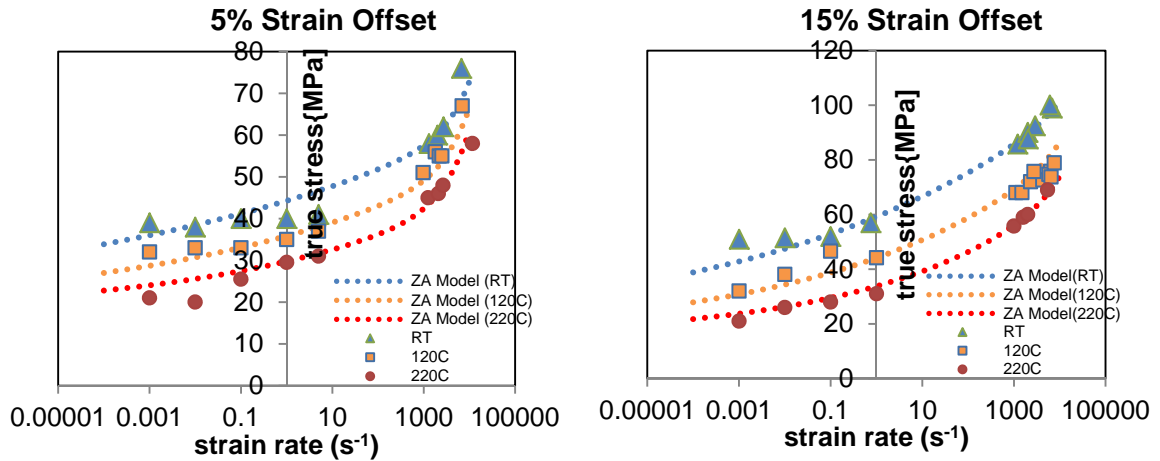


Figure 4.6. Al-0.1%Cu modeled with ZA Model.

#### 4.5 Al-4.5%Cu-0.5%Mg-0.3%Mn-0.3%Ag

Al-4.5%Cu-0.5%Mg-0.3%Mn-0.3%Ag alloy have complete set of experiments in room temperature, 120° C ,and 220° C. Also tests were done at elevated temperatures in 0.001/s strain rate. Modified Johnson-Cook Model and Turkkan-Vural Modified Zerilli-Armstrong Model were used to model the experimental data (Fig 4.7)(Fig. 4.9). Figure 4.8 and Figure 4.10 display the thermal softening behavior captured by the two models.

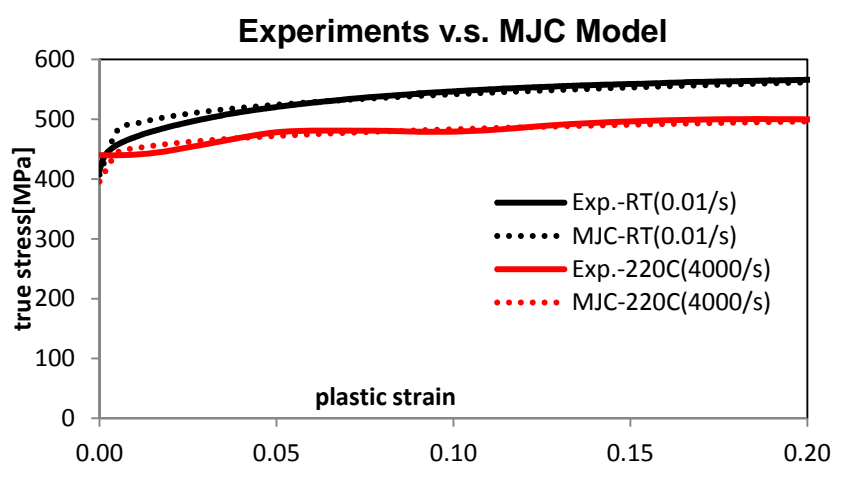
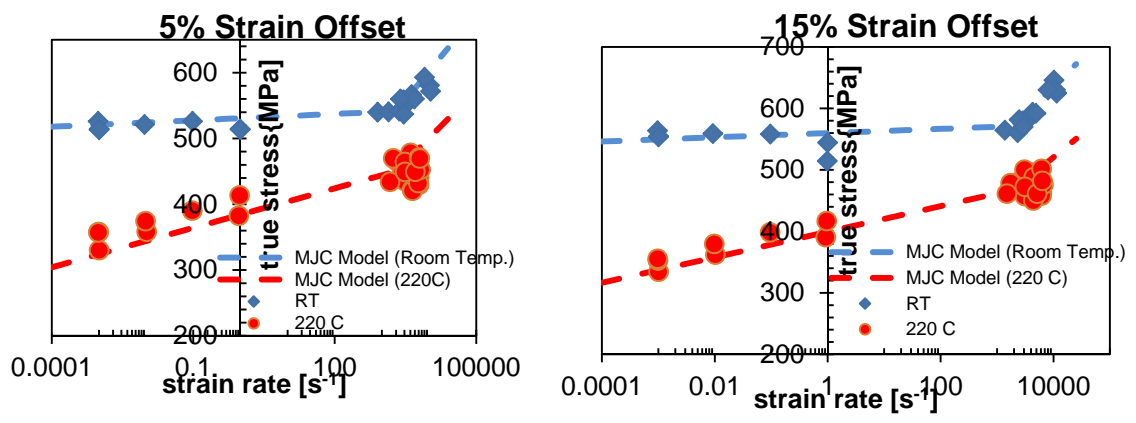


Figure 4.7. Al-4.5%Cu-0.5%Mg-0.3%Mn-0.3%Ag modeled with MJC Model.

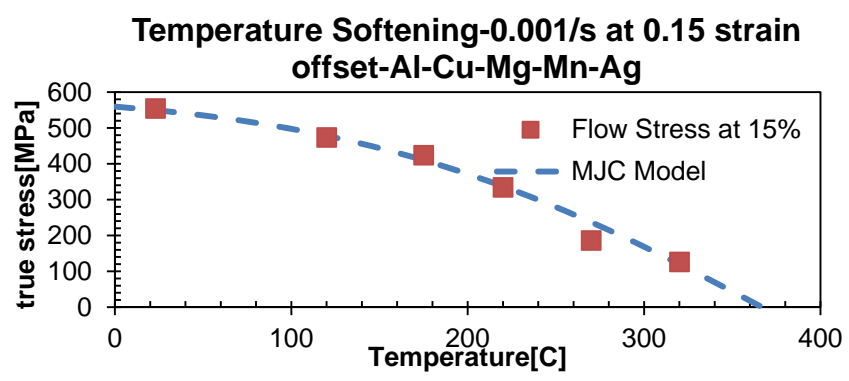


Figure 4.8. Al-4.5%Cu-0.5%Mg-0.3%Mn-0.3%Ag thermal softening captured with MJC Model

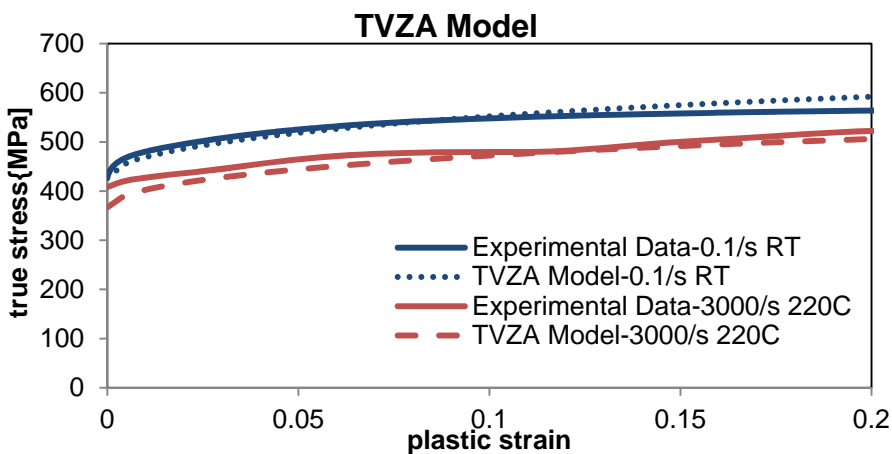
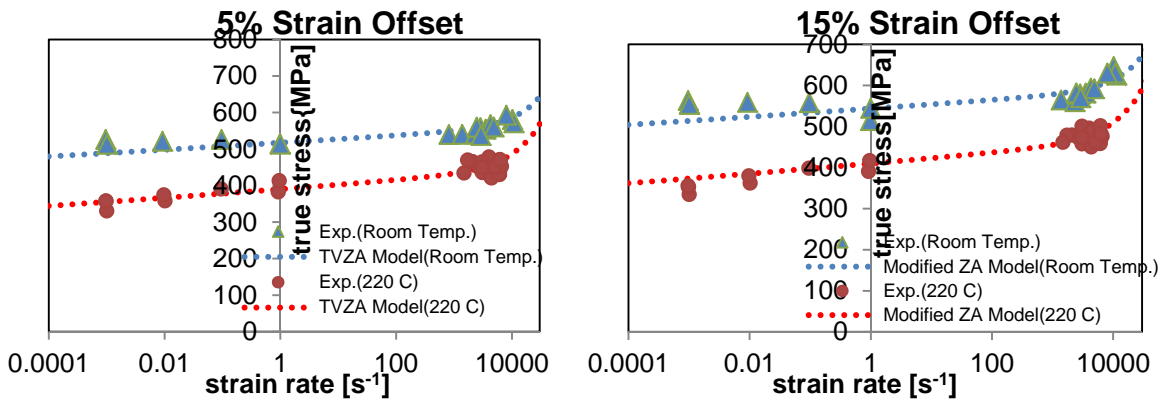


Figure 4.9. Al-4.5%Cu-0.5%Mg-0.3%Mn-0.3%Ag modeled with TVZA Model.

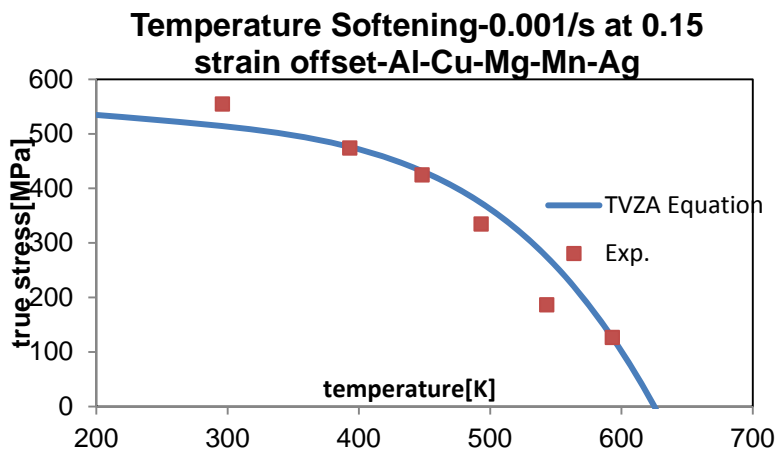


Figure 4.10. Al-4.5%Cu-0.5%Mg-0.3%Mn-0.3%Ag thermal softening captured with TVZA Model

## CHAPTER 5

### ADIABATIC SHEAR BANDING

#### 5.1 Introduction

As discussed at section 1.4, shear-compression specimens (SCS) were used to study adiabatic shear banding on different alloys. The following alloys were tested with SCS:

- Al2139-T8
- Al-4.5%Cu-0.5%Mg-0.3%Mn-0.3%Ag
- Al-4.5%Cu-0.5%Mg-0.3%Mn

#### 5.2 Parameter Fitting

The constants  $k_1$  and  $k_2$  (Eq.1.27 and Eq.1.28) are found by comparing cylindrical non-slotted specimen test with shear-compression specimen test, both of which are carried out at similar quasi-static strain rates.

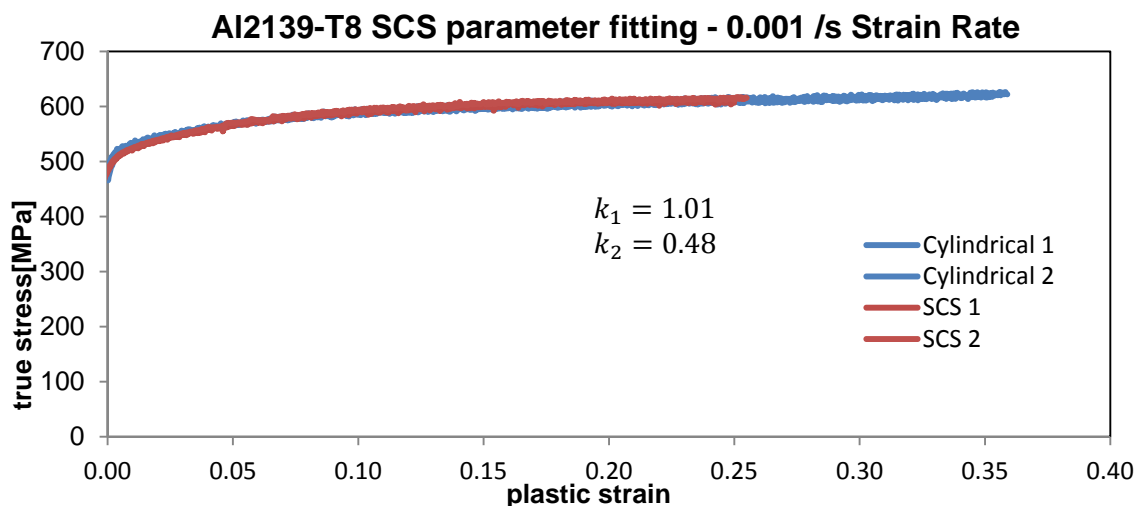


Figure 5.1. Constants  $k_1$  and  $k_2$  are found by comparing quasi-static SCS and cylindrical experimental results.

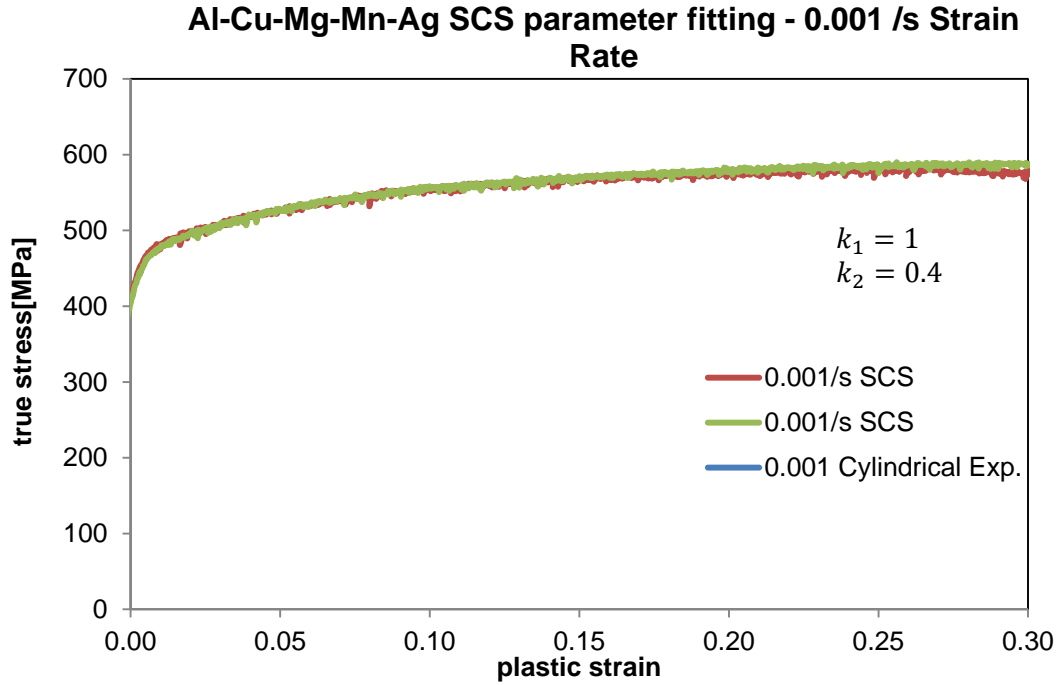


Figure 5.2. Constants  $k_1$  and  $k_2$  are found by comparing quasi-static SCS and cylindrical experimental results.

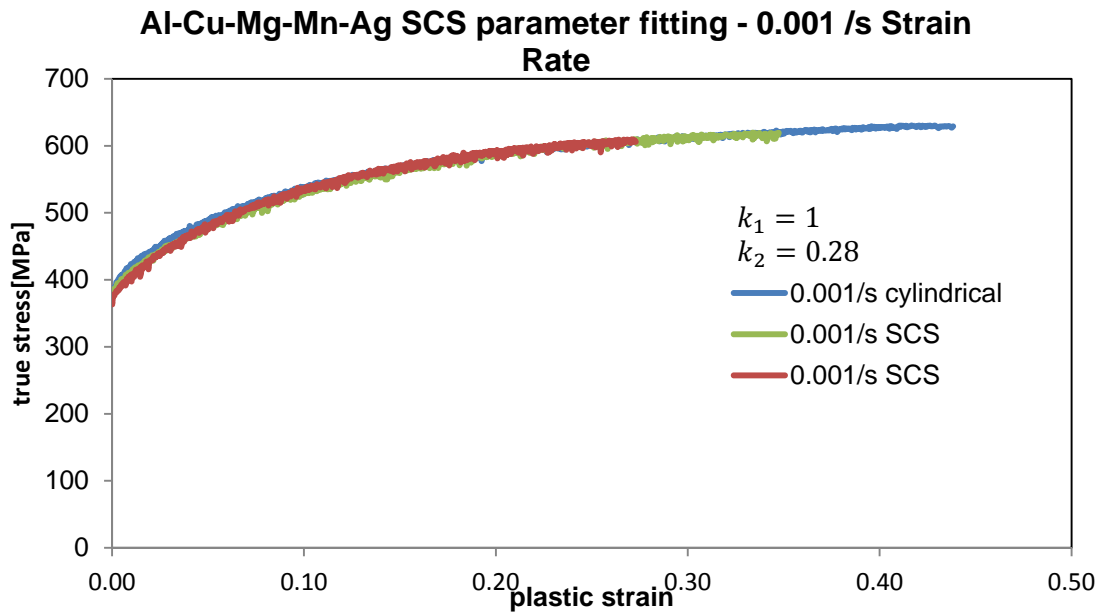


Figure 5.3. Constants  $k_1$  and  $k_2$  are found by comparing quasi-static SCS and cylindrical experimental results.

### 5.3 Dynamic Testing

Three alloys were tested using SHPB in similar strain-rates (Fig 5.4) and Al-4.5%Cu-0.5%Mg-0.3%Mn alloy have shear localization at largest strain (0.45-0.5) value among other alloys. The alloys Al-4.5%Cu-0.5%Mg-0.3%Mn 0.3%Ag and Al2139-T8 show shear localization around 0.35 to 0.4 strain. But these tests are not enough to assess shear localization behaviour of the individual alloys, and therefore stop-ring tests must be done to investigate microstructure during shear localization .

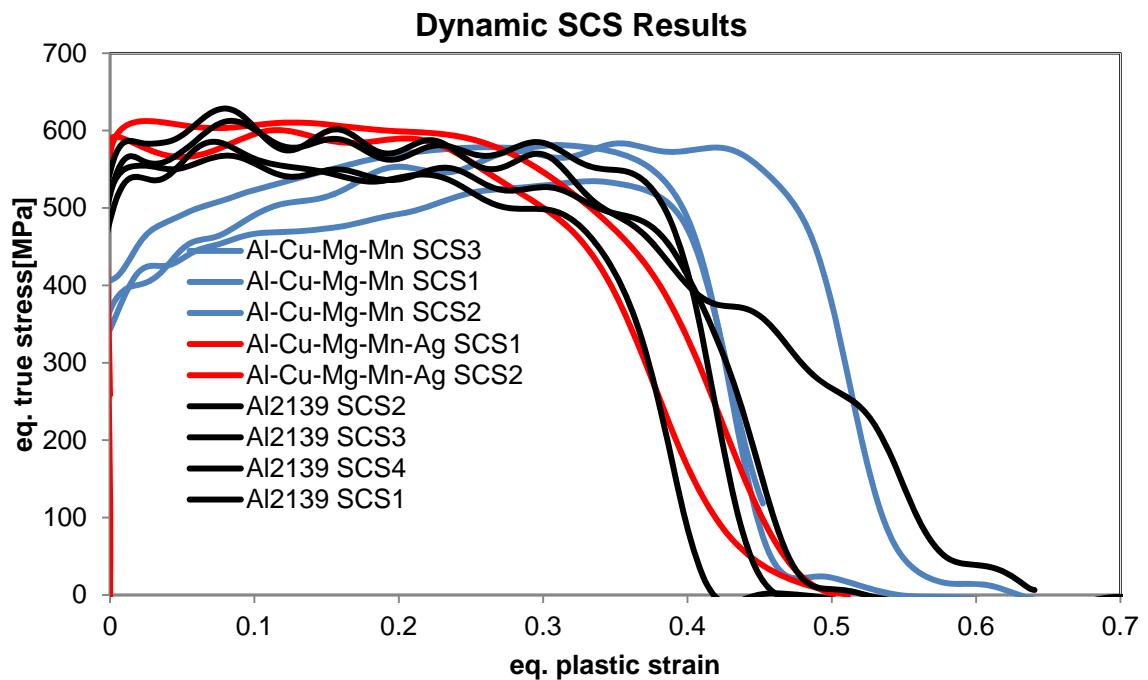


Figure 5.4. SCS results of the three tested alloys. Strain rate is around 4000/s for all tests.

### 5.4 Stop-Ring Testing

To study how shear localization develops in different alloys, dynamic tests need to be stopped at three different points; first at the beginning of the deformation, then just before the shear localization initiates, and finally after the localization point before the fracture. All tests except the ones after localization point are complete (Fig 5.5).

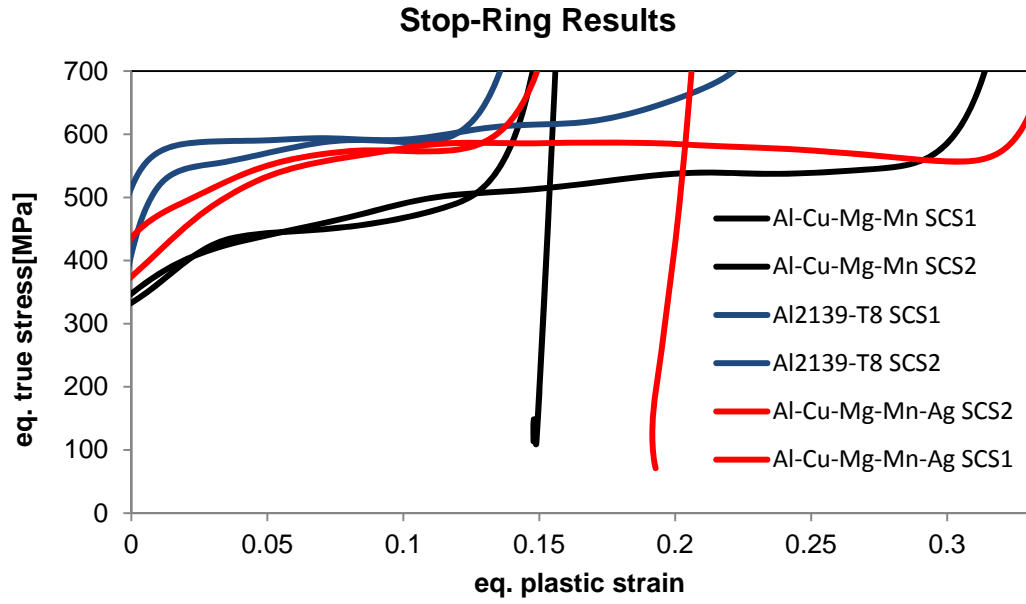


Figure 5.5. Stop-ring SCS results of the three tested alloys. Strain rate is around 4000/s for all tests.

## CHAPTER 6

### DISCUSSION

#### 6.1 Discussion

Current study on the rate and temperature dependent mechanical behavior of Al-Cu material system found out that the Zerilli-Armstrong (ZA) model is not sufficient to model even the simplest aluminum based materials without increased strain rate modification in dynamic regime. After this modification discussed in Section 3.2, the constitutive response of simple materials such as single crystal Al (along [001] and [111] directions), polycrystalline Al, and Al-0.1%Cu can be modeled, but the hardening term in ZA model, which is proportional to the square root of the strain, still remains to be unrealistic for more complex alloys. Even with the Zerilli and Armstrong's alteration of strain hardening, mechanical behavior of more complex precipitation hardened Al-Cu alloys cannot be captured at elevated temperatures due to exponential relation between flow stress and temperature. Current study proposes further modifications to modified ZA Model by incorporating the effect of diffusion and precipitate spacing at elevated temperatures to better capture the thermal softening of flow stress observed in current experiments.

Another objective of this study was to investigate the rate and temperature dependent mechanical behavior of Al-Cu alloy systems and to this end, single crystal Al (along [001] and [111] directions), polycrystalline Al, Al-0.1%Cu, and Al-Cu-Mg-Mn-Ag materials were tested and characterized at room and elevated temperatures. MJC Model and the newly developed TVZA model were proposed to describe rate and temperature dependent constitutive response of these materials. These materials show

similar trends in their material response, such as a distinct change in strain rate sensitivity in quasi-static and dynamic deformation regimes. Also At room temperature and quasi-static rates ( $10^{-3} \text{ s}^{-1}$  to  $10^0 \text{ s}^{-1}$ ), flow stress is almost independent of the stain rate while in dynamic regime there is a significant increase in strain rate sensitivity. However, as the temperature is elevated above room temperature, strain rate dependence is observed even under quasi-static deformation conditions. On the other hand, in dynamic regime ( $10^2 \text{ s}^{-1}$  to  $10^4 \text{ s}^{-1}$ ) temperature does not seem to influence rate sensitivity. This complex behavior was captured with phenomenological MJC Model and the dislocation physics based TVZA Model.

Within the scope of this project, Al-Cu., Al.-Cu.-Mg., Al.-Cu.-Mg.-Mn. alloys were tested at room temperature and due to lack of high temperature data, these alloys have not been characterized with material models.

Last aspect of this study was to assess the ballistic properties of the complex alloys and henceforth, SCS testing was proposed to study the tendency of the alloys to shear localization. SCS results revealed that Al.-Cu.-Mg.-Mn., Al.-Cu.-Mg.-Mn.-Ag. , and Al2139-T8 alloys show shear localization after similar strain values. Furthermore stop ring tests were conducted to better evaluate shear deformation field in these alloys.

## **6.2 Recommendations for Future Work**

The following is recommended for future work for the characterization of aluminum-copper alloy system:

- Complete the elevated temperature tests for the rest of the alloys and then, characterize their material response with MJC and TVZA Models.

- Since the complex materials show adiabatic shear banding and localization at similar strain rates, conduct SCS tests at elevated temperatures to better study the ballistic properties of the complex alloy systems.

## APPENDIX A

### MODELLING PARAMETERS

Table A.1. Modified Johnson-Cook Model parameters for different materials

<b>Material</b>	$q$	$\sigma_0$	$B_0$	$T_0$	$T_m$	$p$	$n$	$C_1$	$C_2$	$\epsilon_{01}$	$\epsilon_t$	$k$
<b>Poly. Al</b>	2.9	14.5	140	175	780	1	0.45	0.0052	0.1565	0.001	20	400
<b>Al-0.1Cu</b>	3.9	5.5	112	41	670	3	0.36	0.0068	0.2065	0.001	150	400
<b>Al-4.5Cu- 0.5Mg-0.3Mn- 0.3Ag</b>	4.5	426	234	0	640	3.9	0.2	0.0027	0.07	0.001	200	400

Table A.2. Zerilli-Armstrong Model parameters for different materials

<b>Material</b>	$\sigma_a$	$A$	$C_0$	$\alpha_1$	$\alpha_2$
<b>Poly. Al</b>	15	424	0.00000158489	0.0044	0.000225
<b>Al-0.1Cu</b>	17	390	0.00000501187	0.0039	0.000175

Table A.3. Turkkan-Vural Modified Zerilli-Armstrong Model parameters for different materials

<b>Material</b>	$\sigma_a$	<b>p</b>	$T_0$	$T_m$	$\omega$	$A$	$C_0$	$\alpha_1$	$\alpha_2$
<b>Al-4.5Cu-0.5Mg- 0.3Mn-0.3Ag</b>	0	4.5	160	625	14	460	0.00001	0.000175	0.0000275

## BIBLIOGRAPHY

- Armstrong, Ronald, and Frank Zerilli. "Dislocation Mechanics Based Analysis Of Material Dynamics Behavior." *Journal De Physique*, 1988.
- Banerjee, Biswajit. "The Mechanical Threshold Stress model for various tempers of AISI 4340 steel." *International Journal of Solids and Structures*, 2007: 834–859.
- Cho, Alex, and Bernard Bes. "Damage Tolerance Capability of an Al-Cu-Mg-Ag Alloy (2139)." *Mater. Sci. Forum.*, 2006: 519-521.
- Elkhodary, K, Lipeng Sun, Douglas Irving, and Donald Brenner. "Integrated Experimental, Atomistic, and Microstructurally Based Finite Element Investigation of the Dynamic Compressive Behavior of 2139 Aluminum." *J. Appl. Mech*, 2009.
- Follansbee, P S, and U F Kocks. "A Constitutive Description of the Deformation of Copper Based on the Use of the Mechanical Threshold Stress as an Internal State Variable." *Acta metallurgica*, 1988: 81-93.
- Follansbee, P S, U F Kocks, and G Regazzoni. "The Mechanical Threshold of Dynamically Deformed Copper and Nitronic 40." *Journal de Physique*, 1985: 25-34.
- Gama, B. A., S. L. Lopatnikov, and J. W. G. Jr. "Hopkinson Bar Experimental Technique: A Critical Review." *Applied Mechanics Reviews*, 2004: 223-249.
- Gray, G. T. "Classic Split Hopkinson Pressure Bar Testing." *ASM Handbook*, 2000: 462-476.
- Johnson, G R, and W H Cook. "A constitutive model and data for metals subjected to large strains, high strain rates and high temperatures." *7th International Symposium on Ballistics*. 1983. 541-547.
- Kocks, U. F. "Laws for Work-hardening and Low Temperature Creep." *Journal of engineering materials and technology*, 1976: 76-85.
- Kocks, U. F. "Realistic constitutive relations for metal plasticity." *Materials Science and Engineering*, 2001: 181-187.
- Meyers, M. A. *Dynamic Behaviour of Materials*. Danvers, MA: John Wiley & Sons, Inc, 1994.

- Placzankis, Brian, and Elizabeth Charleton. "Accelerated Corrosion And Adhesion Assessments Of Carc Prepared Aluminum Alloy 2139-T8 Using Three Various Pretreatment Methods And Two Different Primer Coatings." *DoD Corrosion Conference*. 2009.
- Rittel, D, S Lee, and G Ravichandran. "A shear-compression specimen for large strain testing." *Experimental Mechanics*, 2002: 58-64.
- Rittel, D., G. Ravichandran, and S. Lee. "Large Strain constitutive behaviour of OFHC copper over a wide range strain rates using shear compression specimen." *Mech. Mater*, 2002: 627-642.
- Snyder, David. *Mesoscale Deformation In A 9310 Steel*. M.S. Thesis, Chicago: Illinois Institute of Technology, 2012.
- Tran, Henry. *Rate and temperature dependent mechanical behavior and modeling of Al-Cu alloy system*. MS Thesis, Chicago: Illinois Institute of Technology, 2011.
- Vural, M, A Molinari, and N Bhattacharyya. "Analysis of slot orientation in shear-compression specimen." *Experimental Mechanics*, 2010: 263-273.
- Vural, Murat, and J Caro. "Experimental analysis and constitutive modeling for the newly developed 2139-T8 alloy." *Materials Science and Engineering A*, 2009: 56-65.
- Wright, T. W. *The physics and mathematics of adiabatic shear bands*. Cambridge, U.K: Cambridge University Press, 2002.
- Wulf, G. L. "The high strain rate compression of aluminum." *International Journal of Mechanical Sciences*, 1978: 609-615.
- Zerilli, Frank. "Dislocation Mechanics–Based Constitutive Equations." *METALLURGICAL AND MATERIALS TRANSACTIONS A*, 2004.
- Zerilli, Frank, and Ronald Armstrong. "Dislocation Mechanics Based Constitutive Equation Incorporating Dynamical Recovery and Applied to Thermomechanical Shear Instability." *AIP Conference Proceedings*. 1997. 215-218.
- Zerilli, Frank, and Ronald Armstrong. "Dislocation Mechanics based constitutive relations for material dynamics calculations." *J. Appl. Phys*, 1987.